Supporting Information

Surface Defect-Induced Specific Catalysis Activates 100% Selective Sensing toward Amine Gases at Room Temperature

Wu Wang,[†,#] Taobo Huang,[‖,#] Zhengmao Cao,[‡] Xiuping Zhu,[‖] Yanjuan Sun,[*,†,§] and Fan Dong[*,†,‡,§]

† School of Resources and Environment, University of Electronic Science and Technology of China, Chengdu 611731, P. R. China

‡ Research Center for Carbon-Neutral Environmental & Energy Technology, Institute of Fundamental and Frontier Sciences, University of Electronic Science and Technology of China, Chengdu 611731, P. R. China

§ Yangtze Delta Region Institute (Huzhou), University of Electronic Science and Technology of China, Huzhou 313000, P. R. China

‖ Department of Environmental Science and Engineering, Fudan University, Shanghai 200433, P. R. China

# These authors contributed equally to this work.

*Email: sunyj@uestc.edu.cn

*Email: dfctbu@126.com; dongfan@uestc.edu.cn

Table of Contents

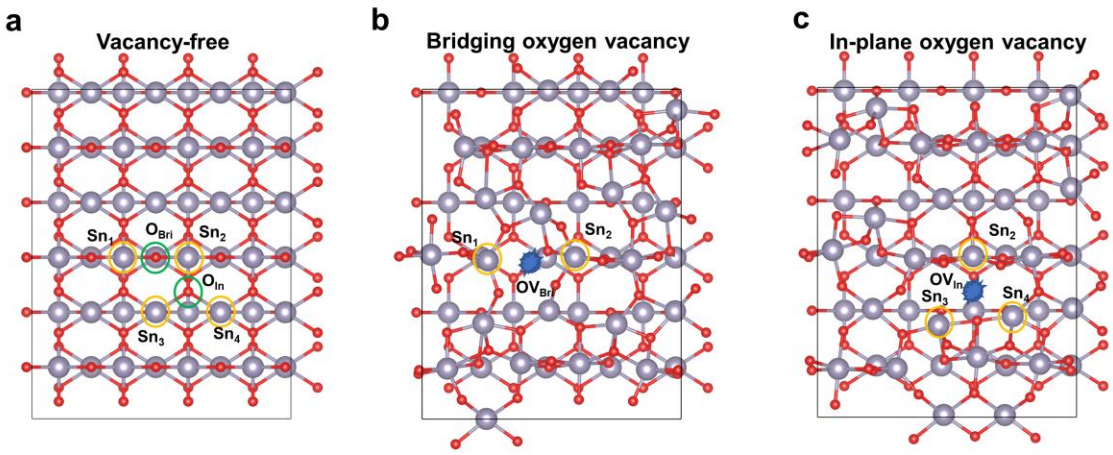

Figure S1. Optimized structures of defect-free SnO_2, SnO_2-OV_{Bri}, and SnO_2-OV_{In}; gray and red balls represent Sn and O atoms, respectively.

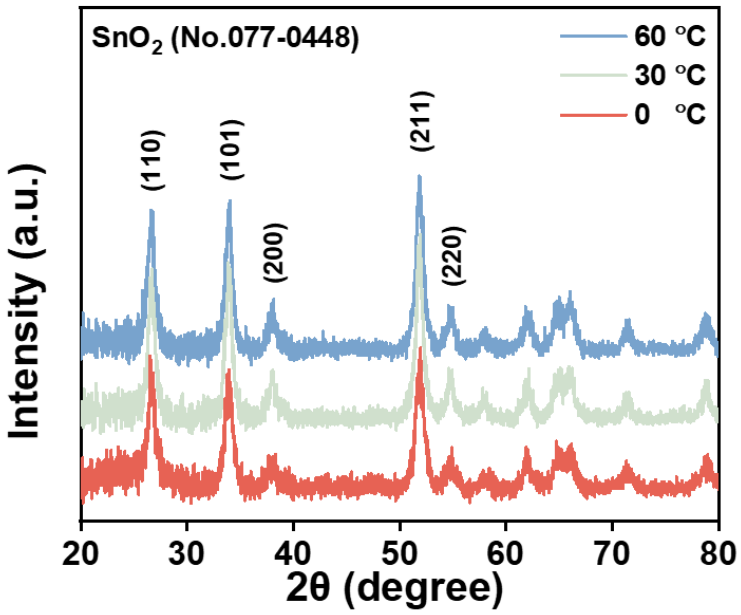

Figure S2. XRD patterns for SnO_2 synthesized under different stirring temperature.

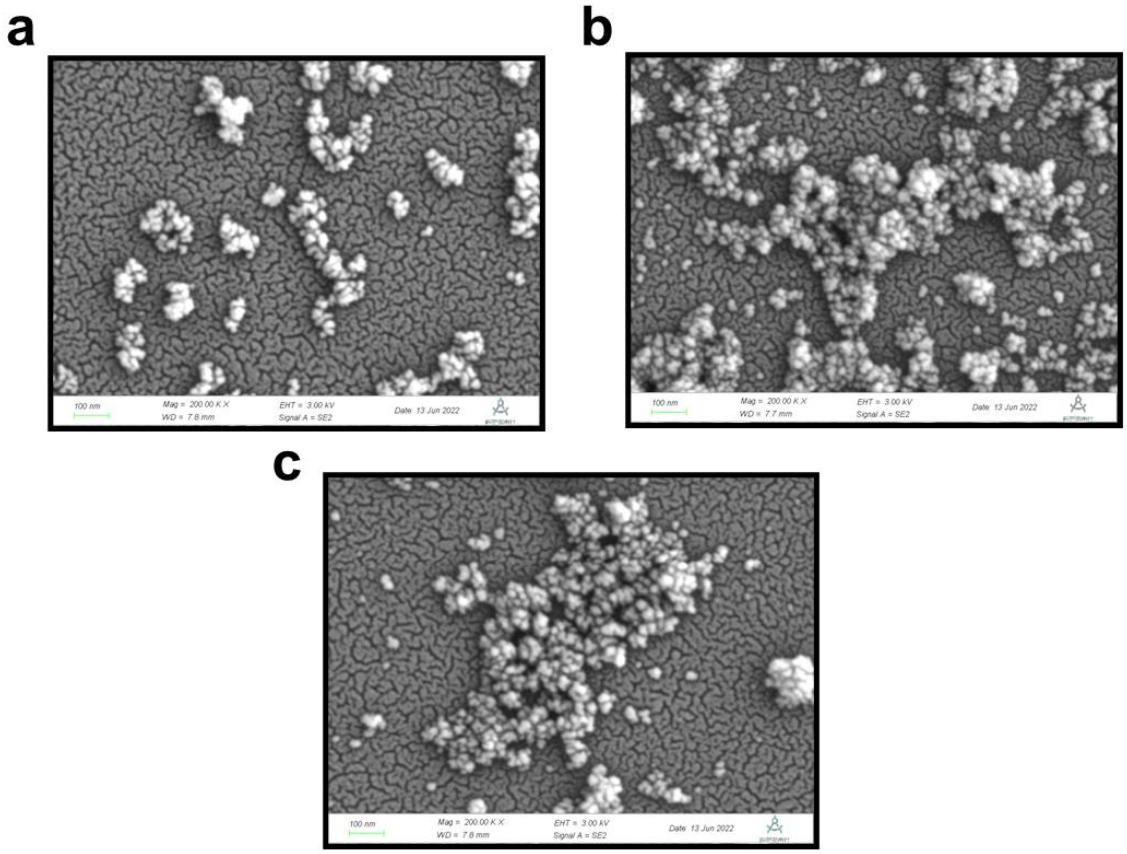

Figure S3. SEM images of SO0 (a), SO3 (b), and SO6 (c).

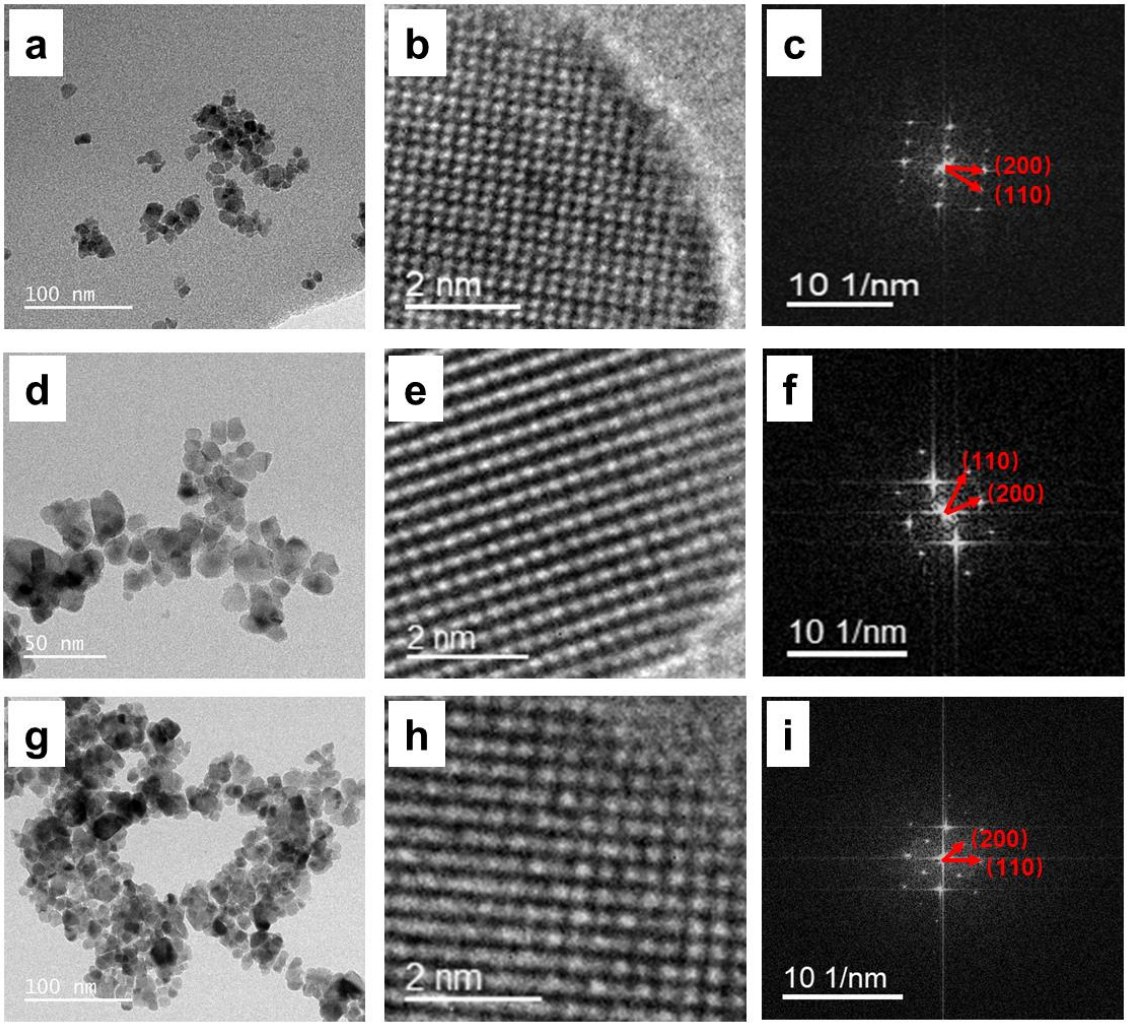

Figure S4. TEM and HRTEM images of SO0 (a-c), SO3 (d-f), and SO6 (g-i).

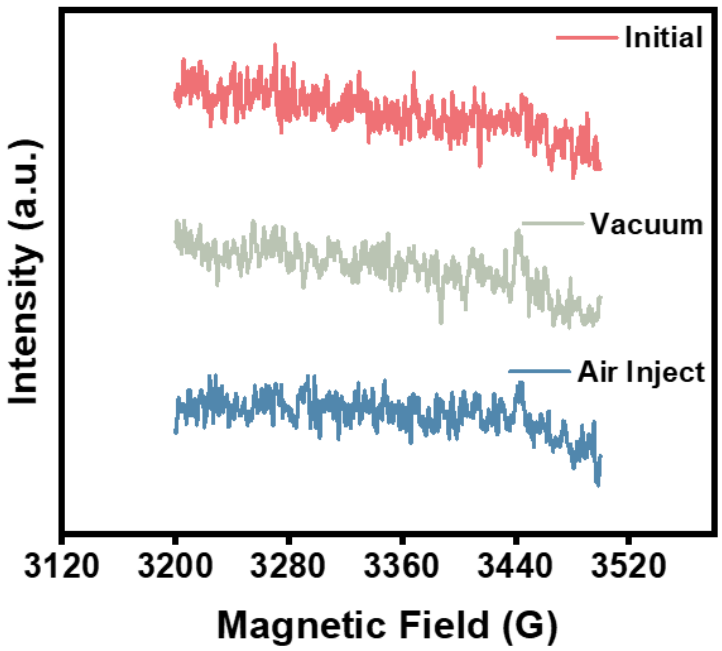

Figure S5. EPR spectra of SO6.

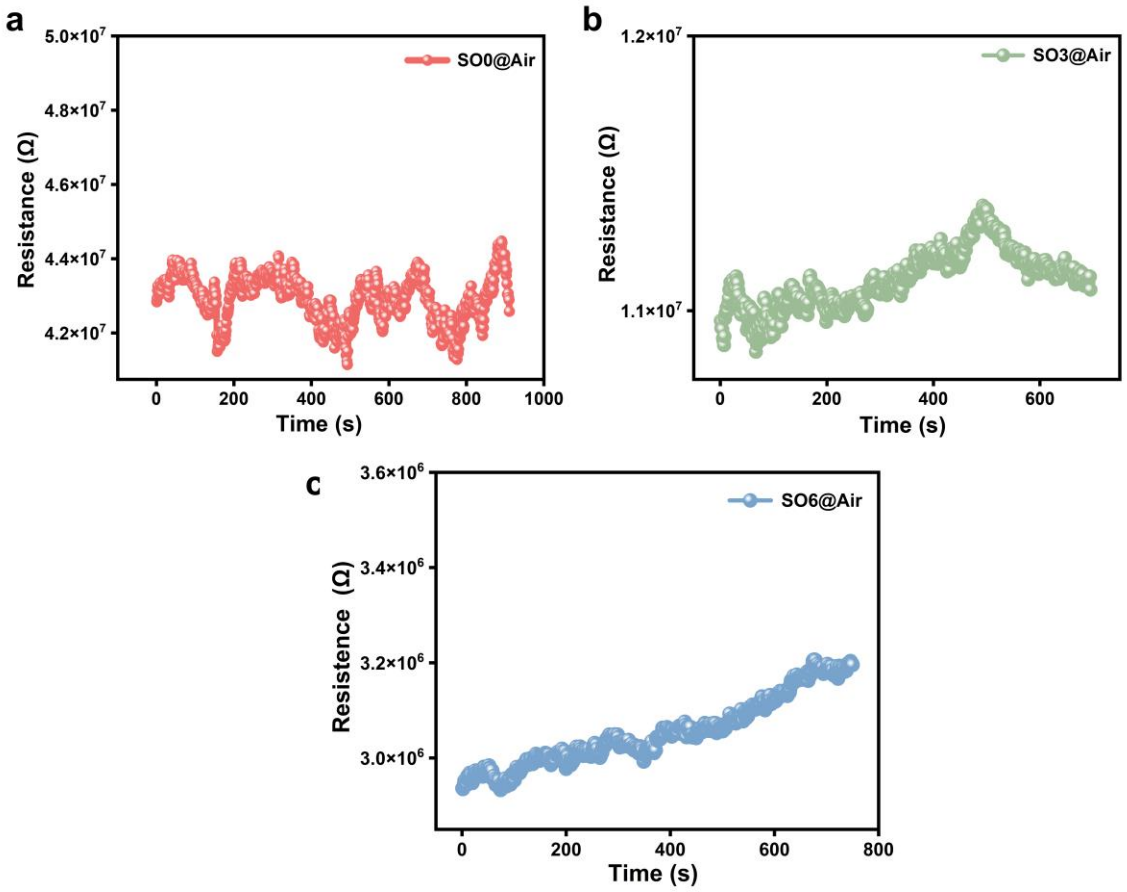

Figure S6. The electrical resistance of SO0 (a), SO3 (b), and SO6 (c) sensors under air atmosphere with 37% relative humidity (RH).

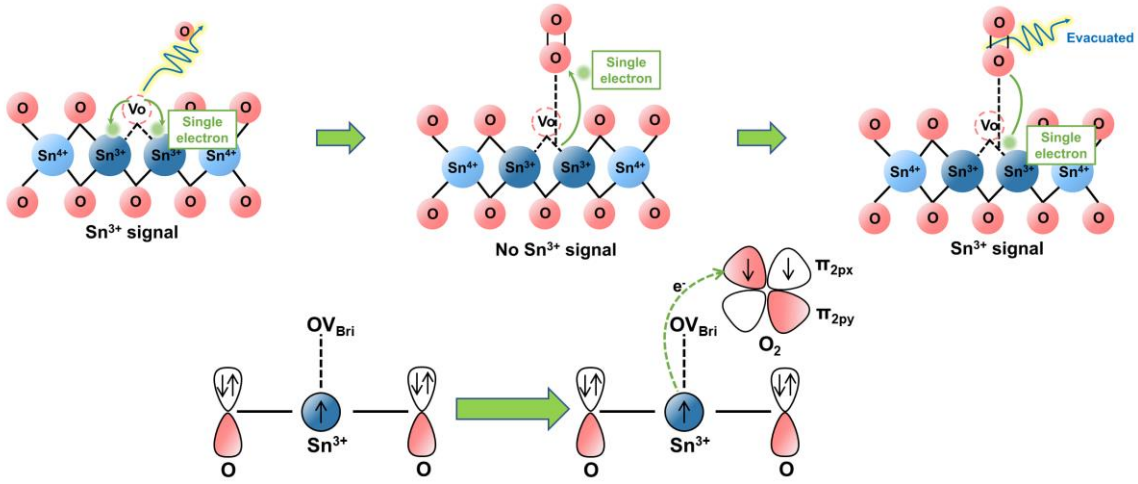

Figure S7. The illustrations of electrons transfer during O_2 adsorption and desorption and the mechanism at an orbital level.

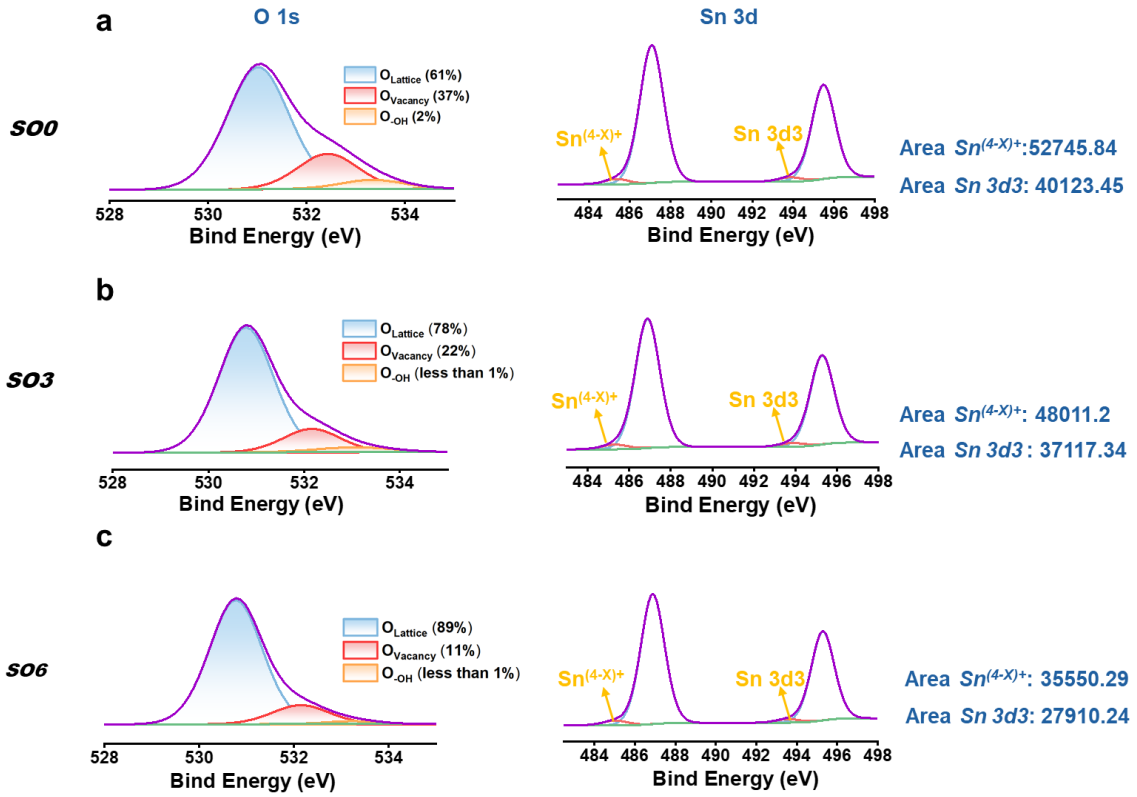

Figure S8. O 1s and Sn 3d XPS spectra generated for SO0 (a), SO3 (b), and SO6 (c).

The corresponding deconvoluted O 1s XPS spectra of three SnO_2 samples are presented in Figure S7a-c. They reveal the existence of three bands at 533.6, 532.3 and 530.7 eV which can be assigned to O atoms from adsorbed hydroxyl species, O atoms surrounding O-vacancy sites and O^{2-} of the metal−oxygen bonds in the SnO_2 lattice [1], respectively. The relative ratio of the O vacancy (highlighted in red) and lattice O in the SO0 sample is 37:61, which is higher than that of the SO3 sample (22:78) and that of the SO3 sample (11:89), indicating that the formation of an oxygen vacancy on SO0 more favorable at lower potentials. Furthermore, two peaks assigned to Sn $3d_{3/2}$ and Sn $3d_{5/2}$ in SO0 show a red shift compared with those in in SO3 and SO6. This lower chemical state of Sn is induced by the oxygen vacancies resulting in a decrease in the number of coordination O atoms [2], which is consistent with the obvious peaks at 485.1 eV ($Sn^{(4-x)+}$) in SO0.

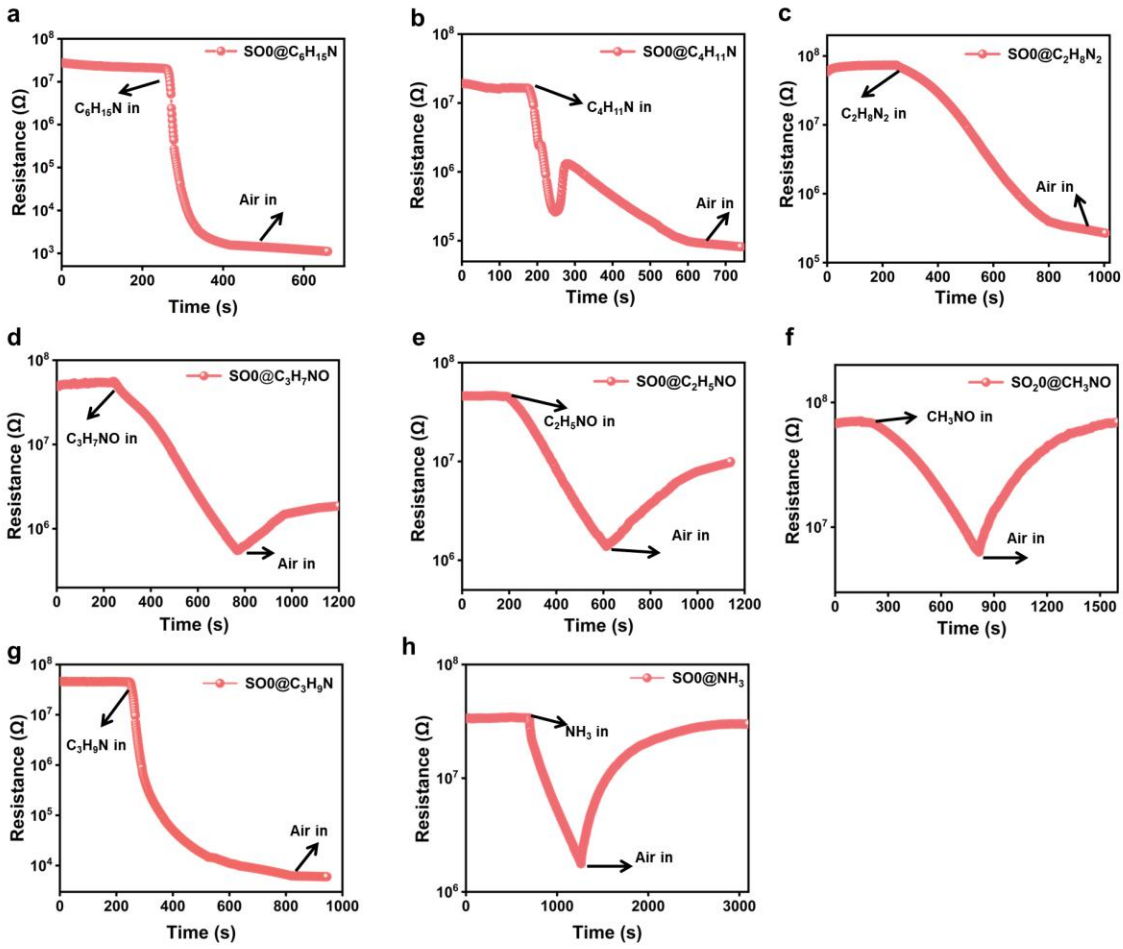

Figure S9. Responses of SO0 sensor towards 100 ppm of triethylamine (a), diethylamine (b), ethanediamine (c), dimethylformamide (d), methylformamide (e), formamide (f), trimethylamine (g), and ammonia (h) at room temperature and 37-41% RH.

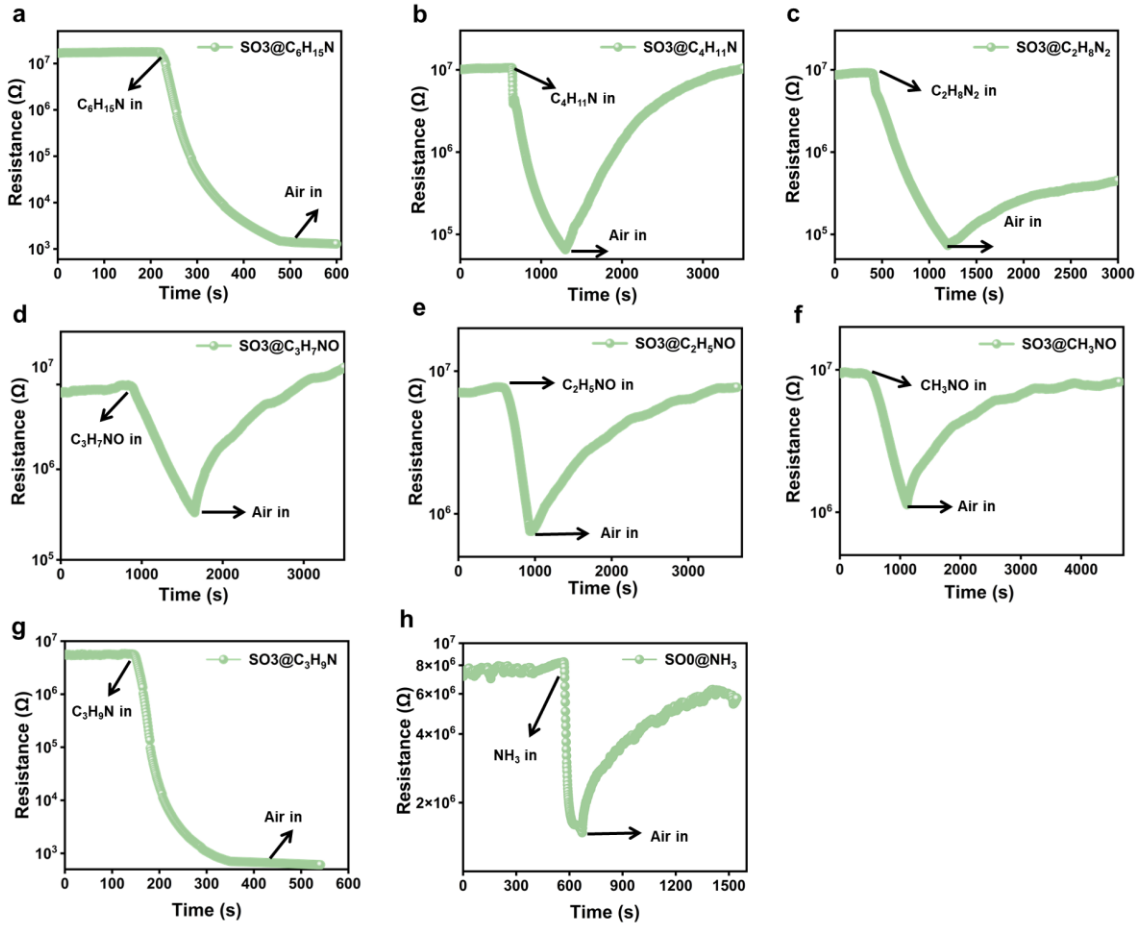

Figure S10. Responses of SO3 sensor towards 100 ppm of triethylamine (a), diethylamine (b), ethanediamine (c), dimethylformamide (d), methylformamide (e), formamide (f), trimethylamine (g), and ammonia (h) at room temperature and 38-39% RH.

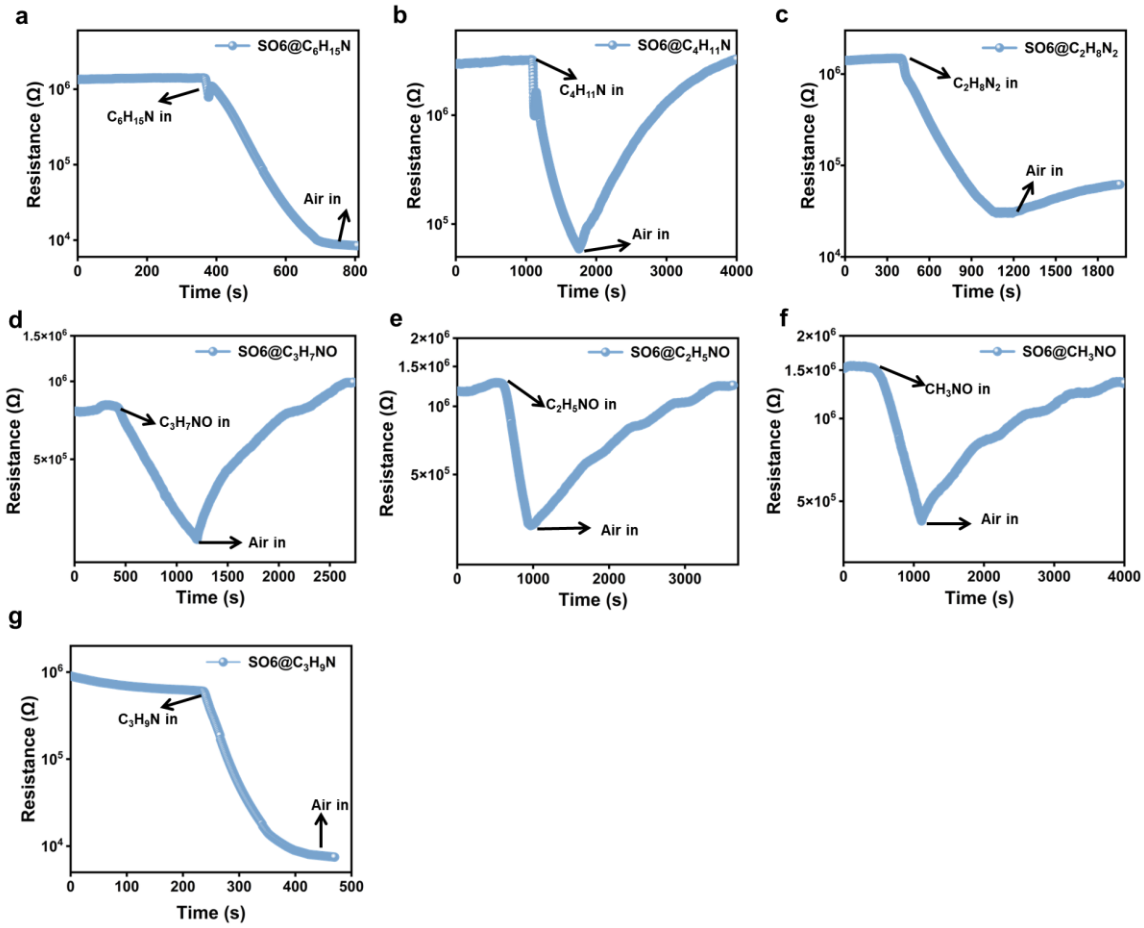

Figure S11. Responses of SO6 sensor towards 100 ppm of triethylamine (a), diethylamine (b), ethanediamine (c), dimethylformamide (d), methylformamide (e), formamide (f), and trimethylamine (g) at room temperature and 35-39%$_{RH}$.

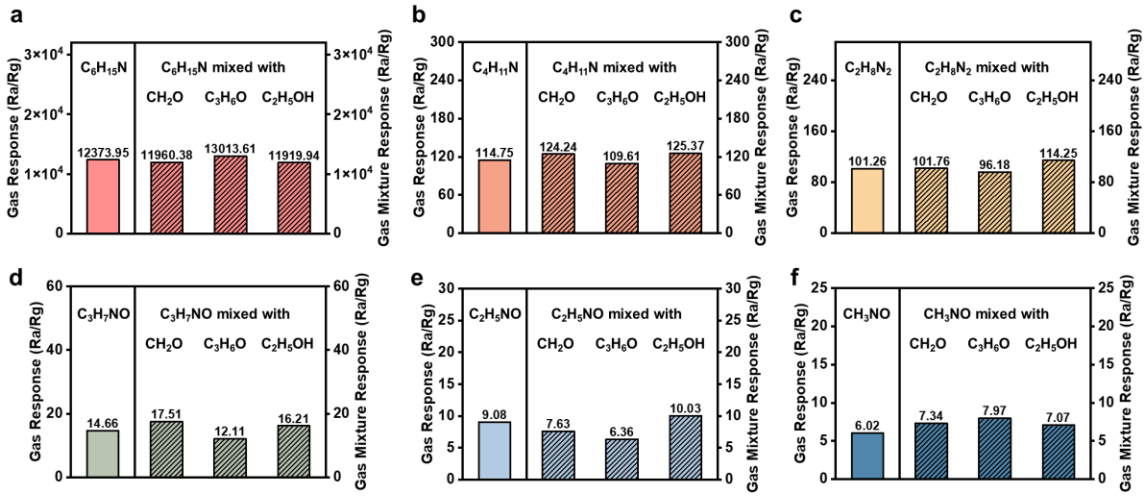

Figure S12. Gas responses of SO3 sensor towards 100 ppm of each amine gas: triethylamine (a), diethylamine (b), ethanediamine (c), dimethylformamide (d), methylformamide (e), and formamide (f) mixing with 10 ppm of methanal, acetone and ethanol, respectively (at room temperature and 39-41% RH).

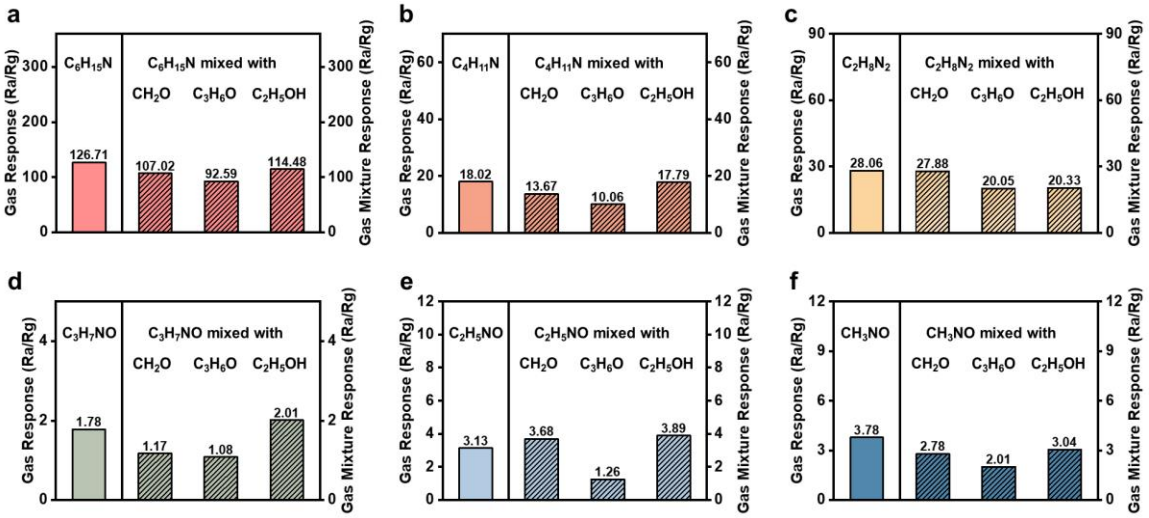

Figure S13. Gas responses of SO6 sensor towards 100 ppm of each amine gas: triethylamine (a), diethylamine (b), ethanediamine (c), dimethylformamide (d), methylformamide (e), and formamide (f) mixing with 10 ppm of methanal, acetone and ethanol, respectively (at room temperature and 39-41% RH).

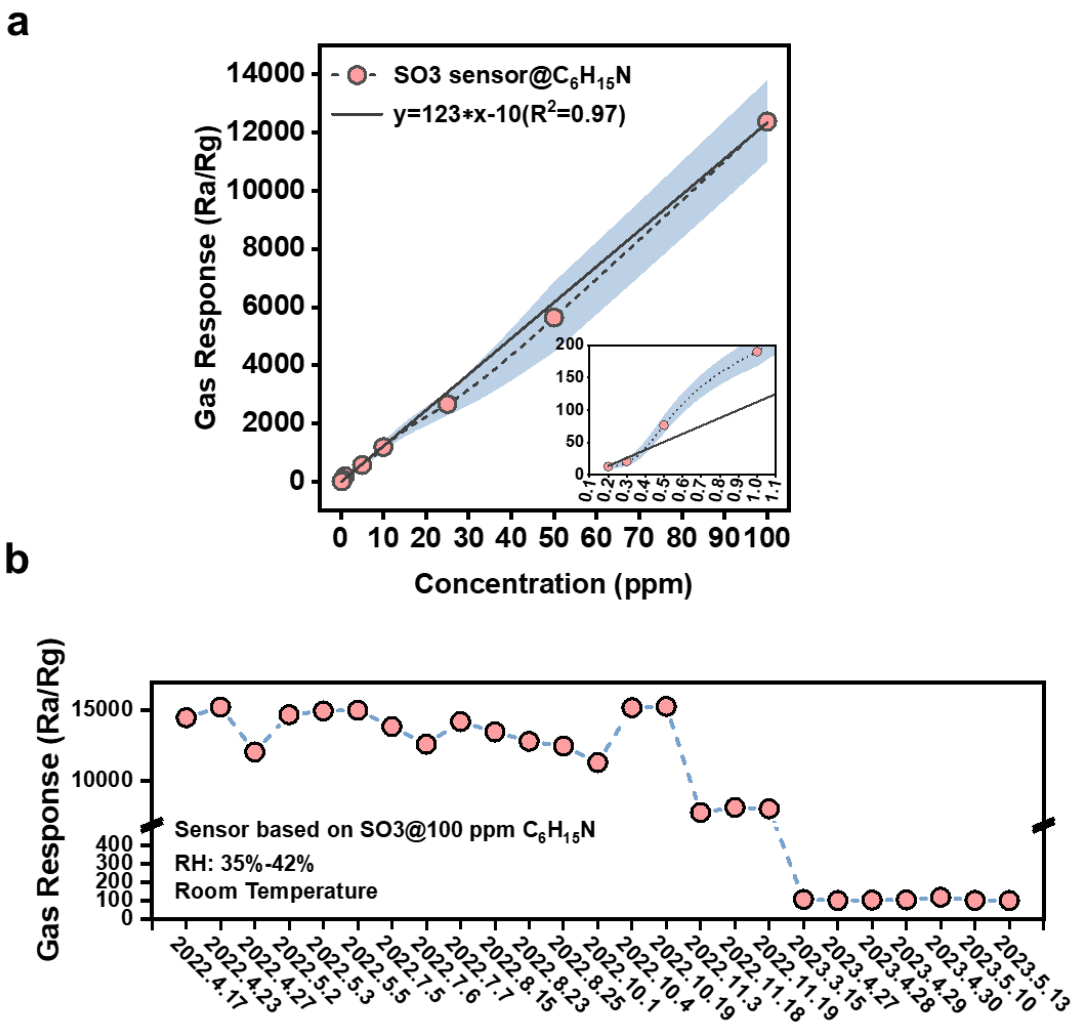

Figure S14. The long-term stability of the SO3 sensor under a room-temperature and 35-42% RH conditions towards 100 ppm of triethylamine and its limit of detection.

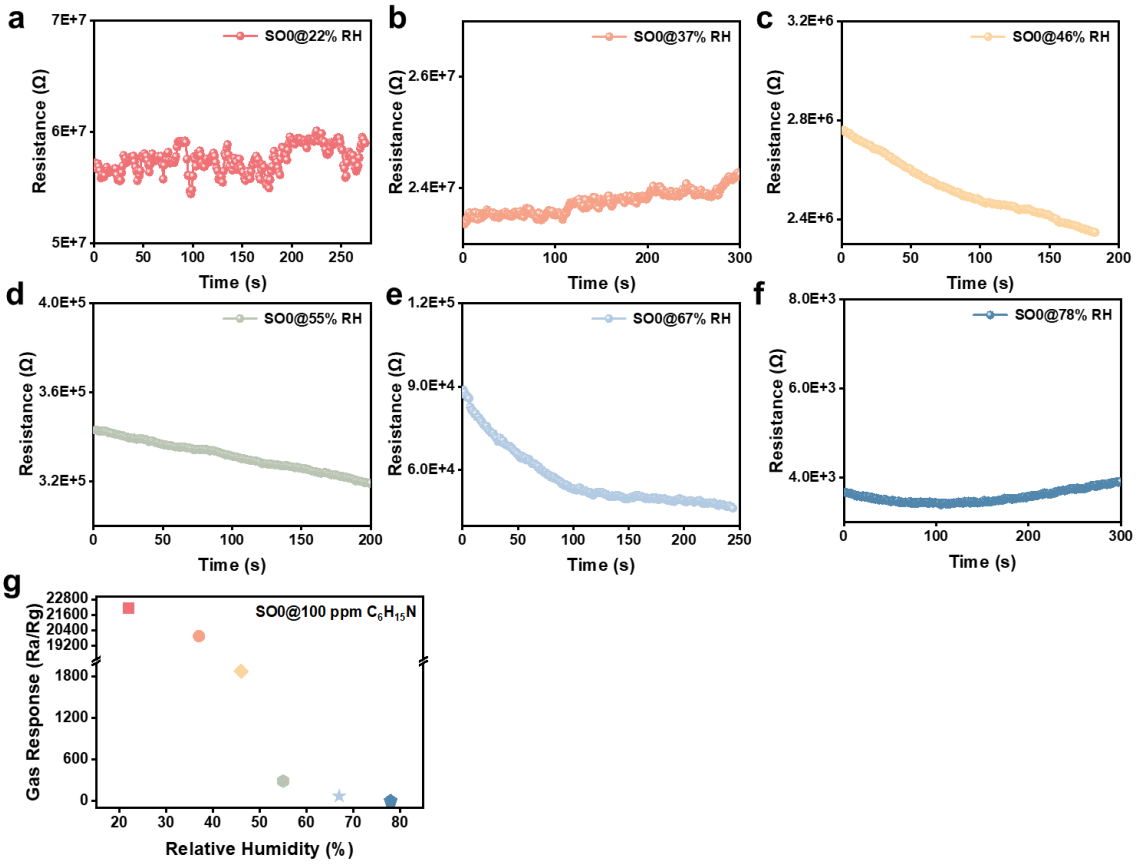

Figure S15. The baseline resistance of SO0 sensor at room temperature and under 22% RH (a), 37% RH (b), 46% RH (c), 55% RH (d), 67% RH (e), and 78% RH (f); (g) Gas responses of SO0 sensor towards 100 ppm triethylamine gas at room temperature and under corresponding relative humidity.

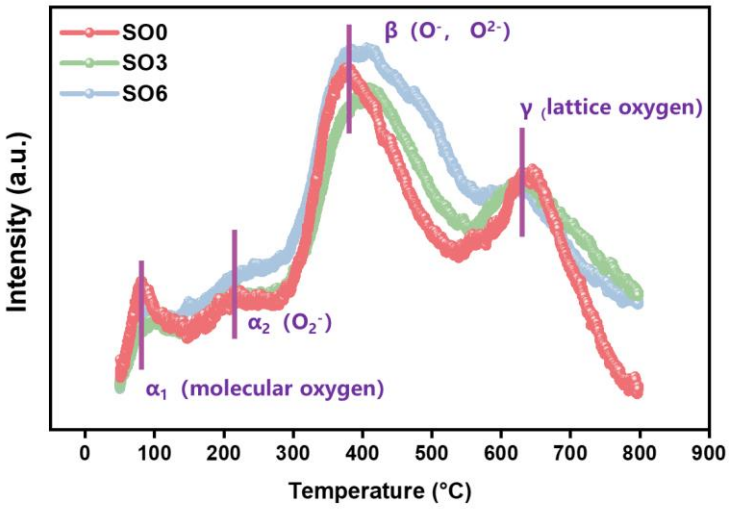

	α-Quantity (mmol/g)	α-Peak Active Gas Flow Rate (mmol/min)
SO0	$1.100e^{-2}$	$2.120e^{-4}$
SO3	$9.037e^{-3}$	$2.120e^{-4}$
SO6	$6.279e^{-3}$	$1.403e^{-4}$

Figure S16. O_2-TPD spectra of SO0, SO3 and SO6.

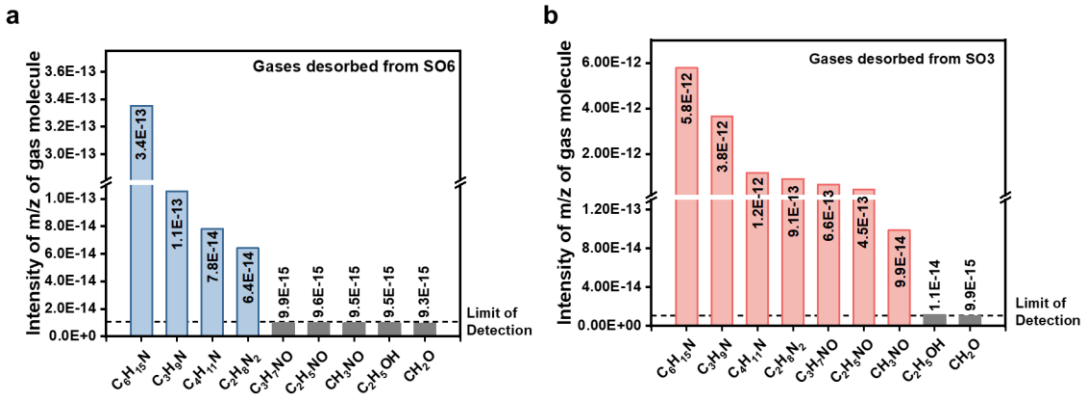

Figure S17. The absolute intensity of the mass-to-charge ratio (m/z) of each gas molecule after desorption from the SO6 (a) and SO3 (b) by CAD-MS measurements.

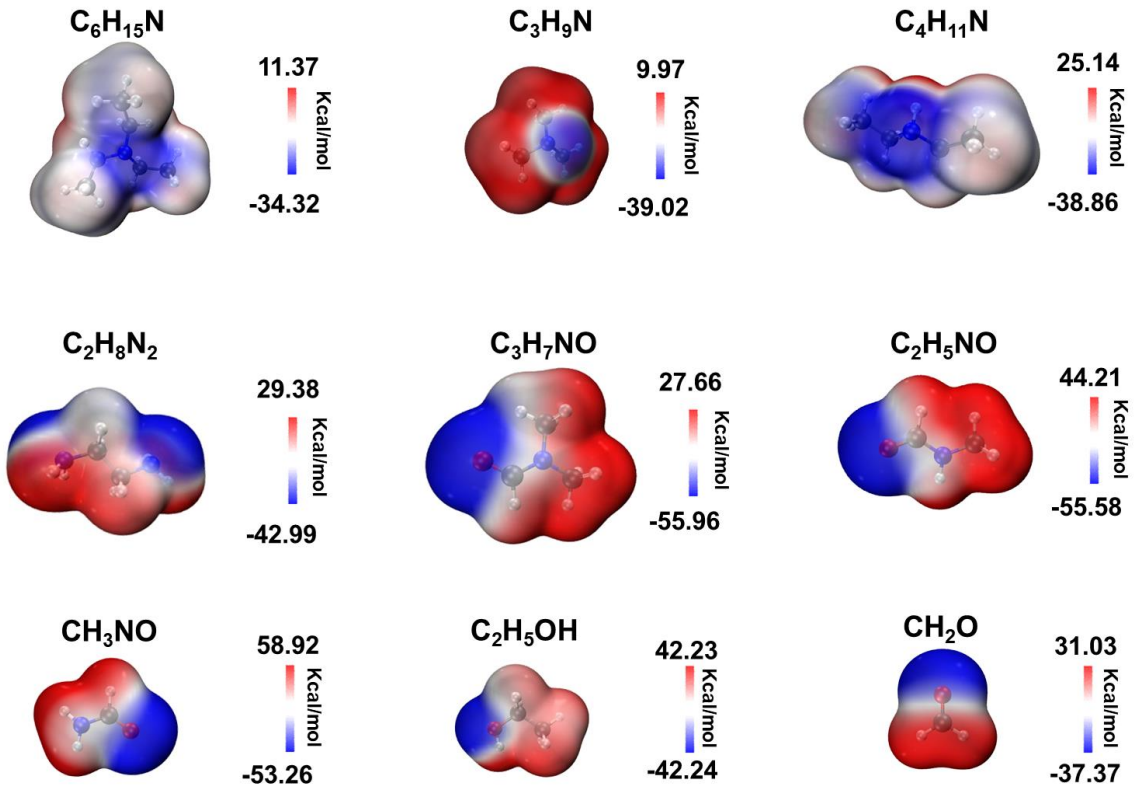

Figure S18. Electrostatic potential of triethylamine, trimethylamine, diethylamine, ethanediamine, dimethylformamide, methylformamide, formamide, ethanol, and methanal molecules.

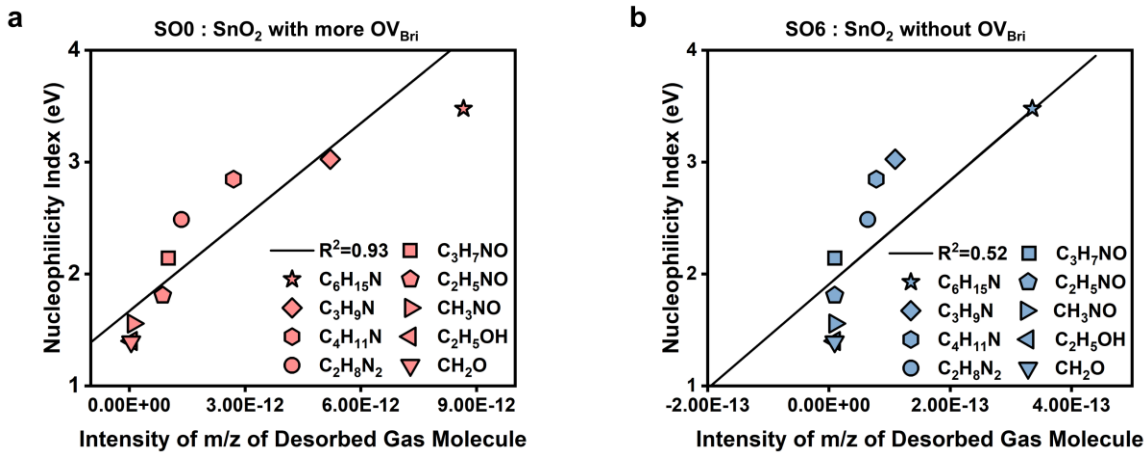

Figure S19. Linear fitting curve of nucleophilicity index (N_{Nu}) of nine testing gases and intensity of the mass-to-charge ratio (m/z) of each gas molecule desorbed from SO0 (a) and SO6 (b).

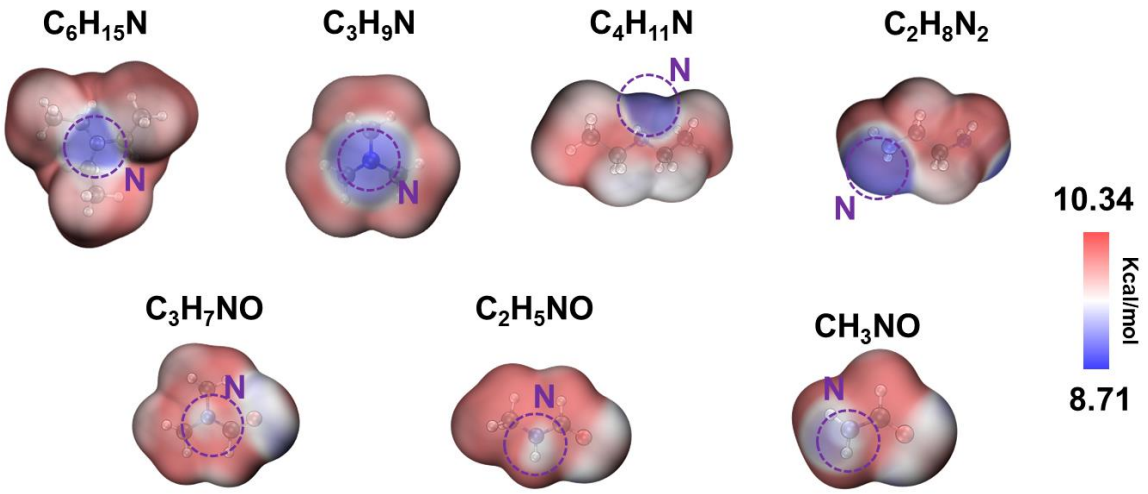

Figure S20. The average localized ionization energy (ALIE) of seven amine molecules.

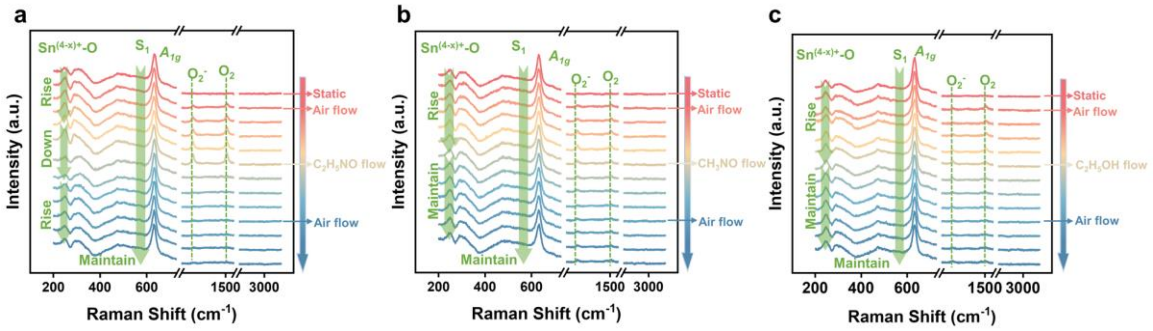

Figure S21. (a-c) *In situ* Raman spectra of methylformamide-, formamide-, and ethanol-sensing reactions on SO0.

No Raman features about targeted gases can be observed from these three sensing processes.

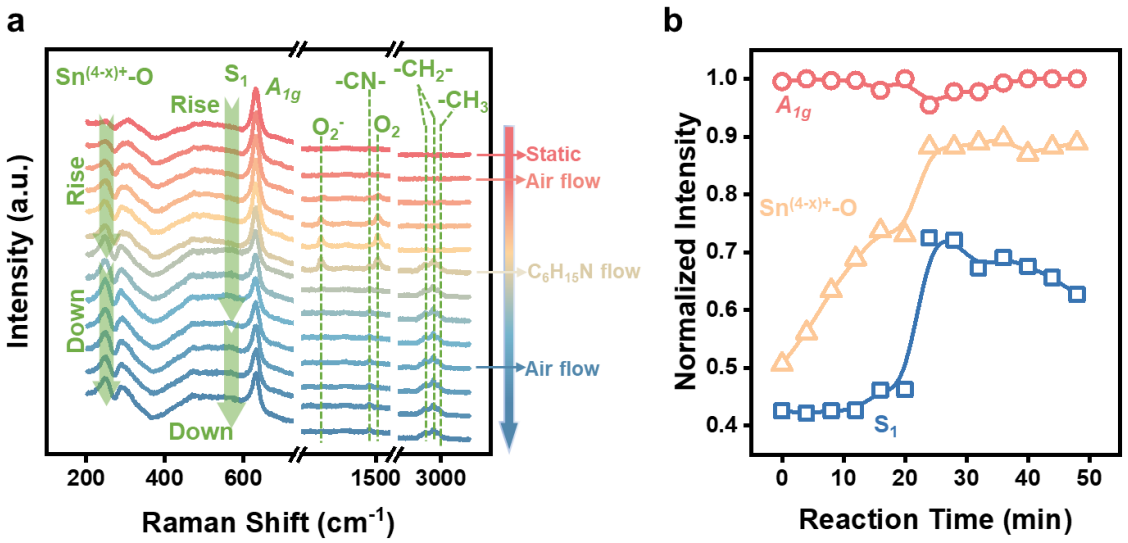

Figure S22. (a) *In situ* Raman spectra of triethylamine sensing reaction on SO3; (b) Evolution of A_{1g} and S_1 modes and $Sn^{(4-x)+}$-O vibration during this reaction.

It is observed in the above figure that two peaks at 2892 cm^{-1} and 2876 cm^{-1} are attributed to $-CH_2-$, one single peak at 2937 cm^{-1} attributed to $-CH_3$ and one single peak at 1457 cm^{-1} is attributed to $-CN-$ [3], which indicates the obvious adsorption of triethylamine molecules on SO3 surface. The Raman features about oxygen species are same as that in triethylamine-sensing processes on SO0.

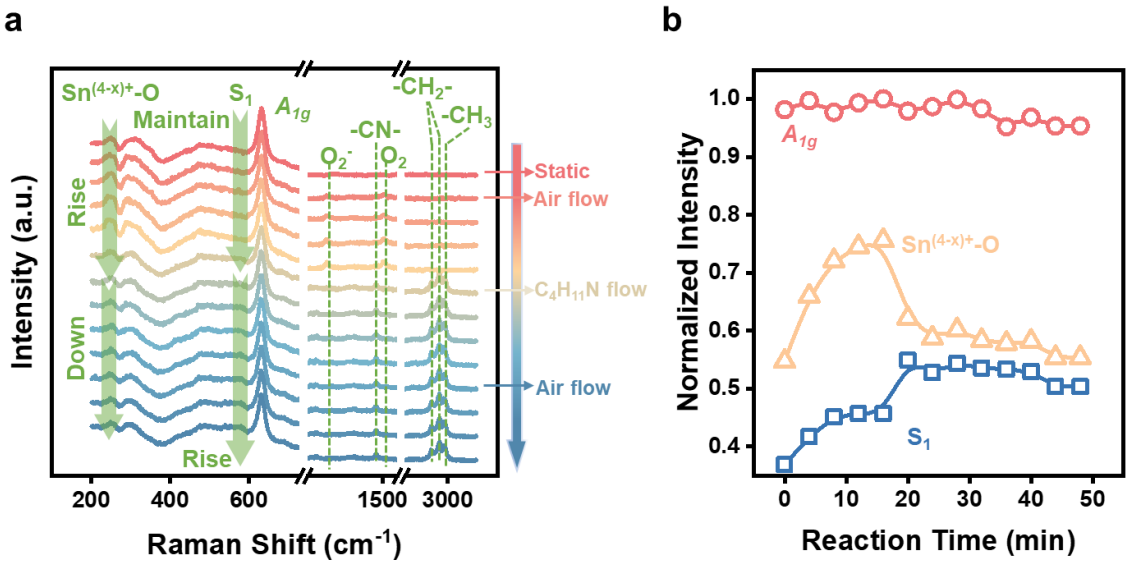

Figure S23. (a) *In situ* Raman spectra of diethylamine sensing reaction on SO3; (b) Evolution of A_{1g} and S_1 modes and $Sn^{(4-x)+}$-O vibration during this reaction.

It is observed in the above figure that two peaks at 2887 cm^{-1} and 2871 cm^{-1} are attributed to $-CH_2-$, one single peak at 2937 cm-1 attributed to $-CH_3$ and one single peak at 1465 cm^{-1} is attributed to $-CN-$ [4] , which indicates the obvious adsorption of diethylamine molecules on SO3 surface. The Raman features about oxygen species are same as that in triethylamine-sensing processes on SO0.

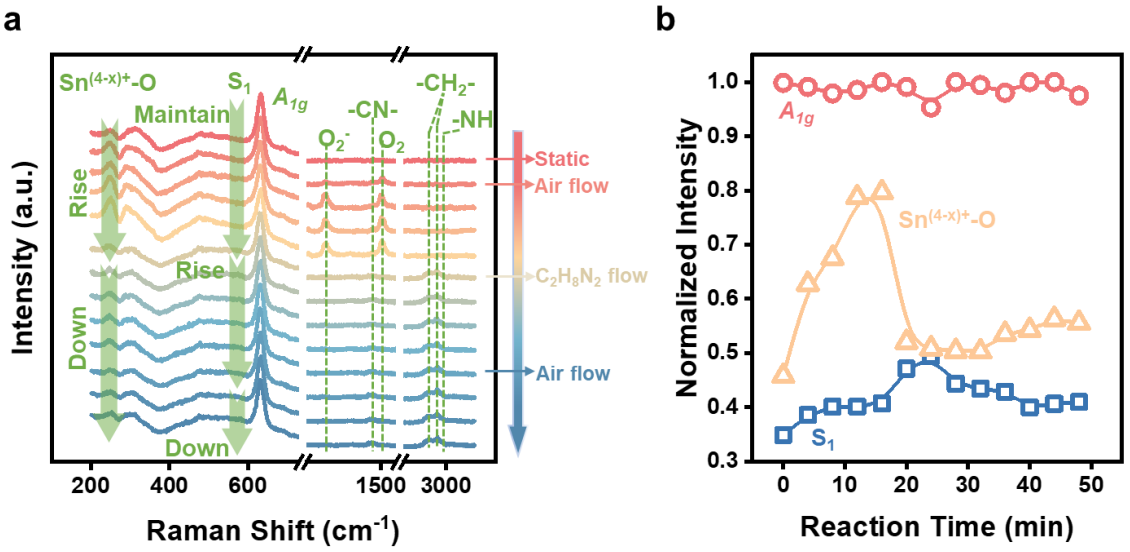

Figure S24. (a) *In situ* Raman spectra of ethanediamine sensing reaction on SO3; (b) Evolution of A_{1g} and S_1 modes and $Sn^{(4-x)+}$-O vibration during this reaction.

It is observed in the above figure that two peaks at 2857 cm^{-1} and 2917 cm^{-1} are attributed to $-CH_2-$, one single peak at 2925 cm^{-1} attributed to −NH and one single peak at 1466 cm^{-1} [1] is attributed to −CN− [5] , which indicates the obvious adsorption of ethanediamine molecules on SO3 surface. The Raman features about oxygen species are same as that in triethylamine-sensing processes on SO0.

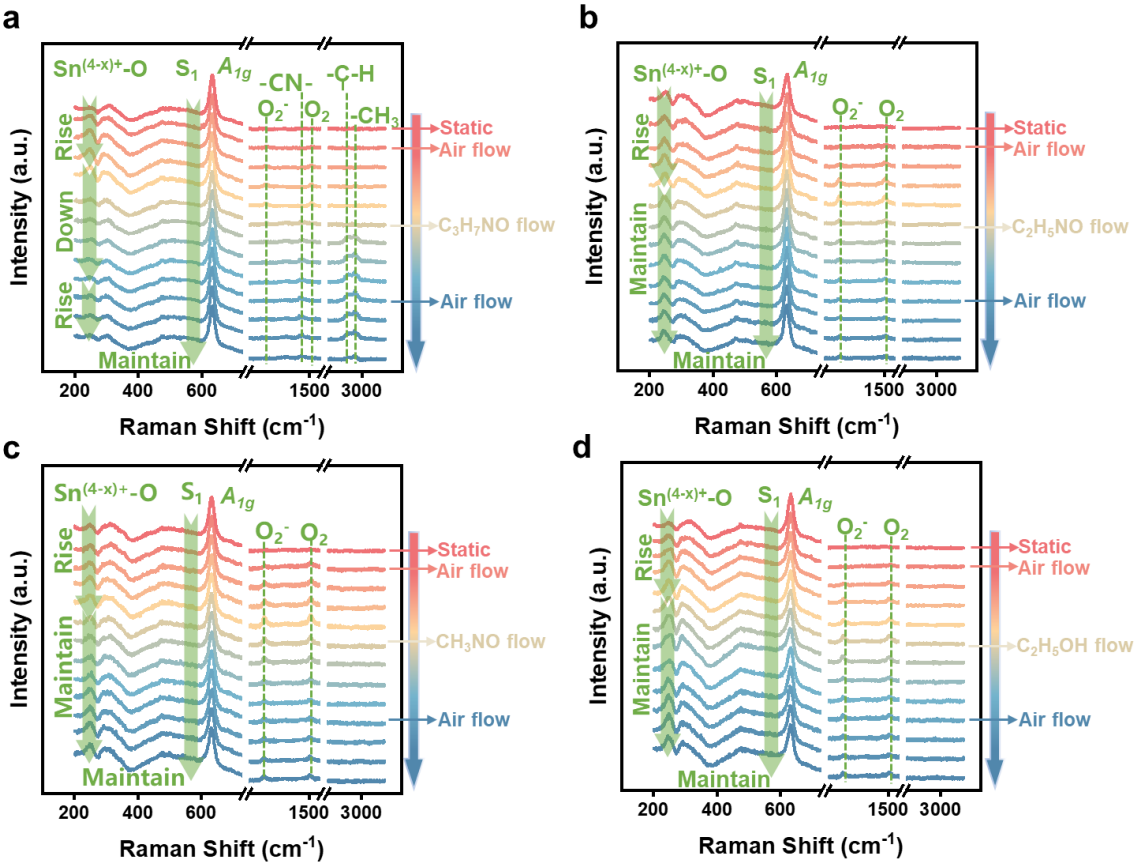

Figure S25. *In situ* Raman spectra of dimethylformamide (a), methylformamide (b), formamide (c), and ethanol (d) sensing reactions on SO3.

It is observed in Figure S22a that one single peak at 2852 cm^{-1} are attributed to $U_{C\text{-}H}$, one single peak at 2931 cm^{-1} attributed to $-CH_3$ and one single peak at 1437 cm^{-1} is attributed to $-CN-$ [6], which indicates the obvious adsorption of dimethylformamide molecules on SO3 surface. The Raman features about oxygen species from these four sensing processes are same as that in triethylamine-sensing processes on SO0.

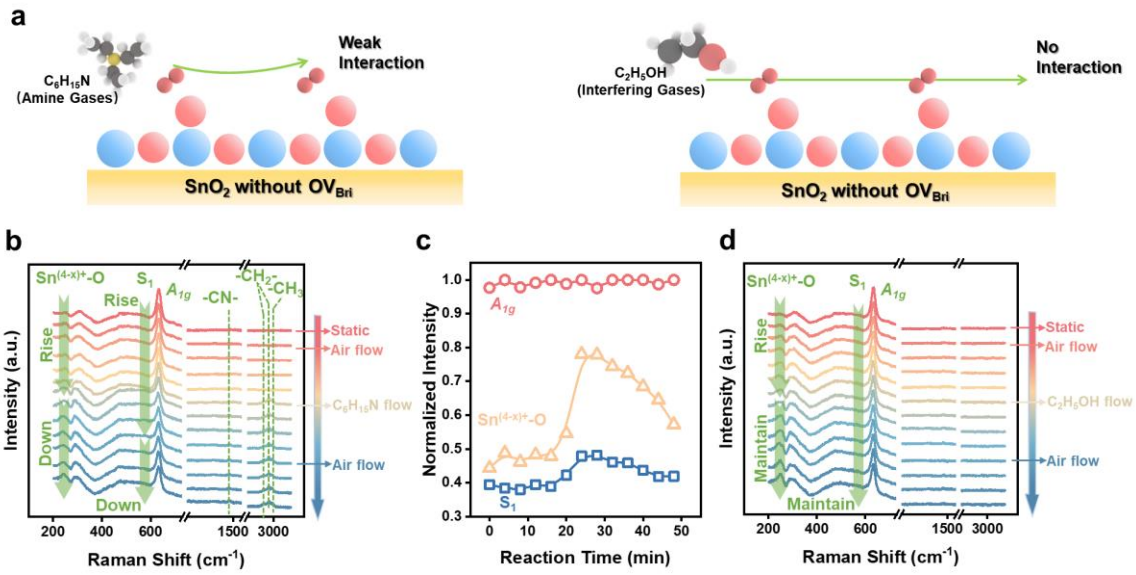

Figure S26. (a) Schematic diagram illustrating non-specific reaction on SO6 for amine gases (triethylamine chosen as a representative amine gas and ethanol chosen as a representative interfering gas); (b) *In situ* Raman spectra of triethylamine sensing reaction on SO6; (c) Evolution of A_{1g} and S_1 modes and $Sn^{(4-x)+}$-O vibration during this reaction; (d) *In situ* Raman spectra of ethanol sensing reaction on SO6.

It is observed in Figure S23b that two peaks at 2892 cm^{-1} and 2876 cm^{-1} are attributed to $-CH_2-$, one single peak at 2965 cm^{-1} attributed to $-CH_3$ and one single peak at 1461 cm^{-1} is attributed to $-CN-$ [3] which indicates the obvious adsorption of triethylamine molecules on SO6 surface. No Raman features about oxygen species can be observed from these two sensing processes.

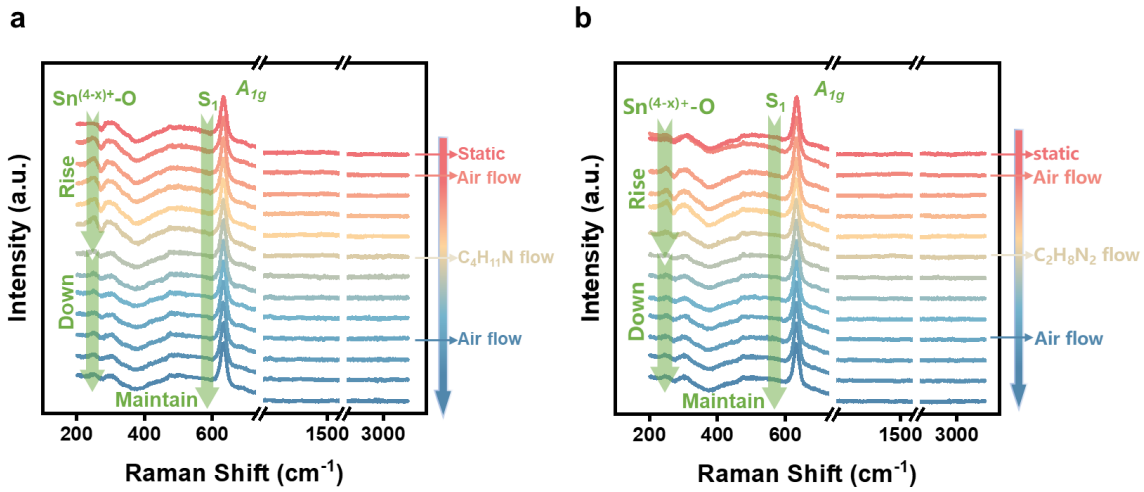

Figure S27. *In situ* Raman spectra of diethylamine (a) and ethanediamine (b) sensing reactions on SO6.

No Raman features about targeted gases and oxygen species can be observed from these two sensing processes.

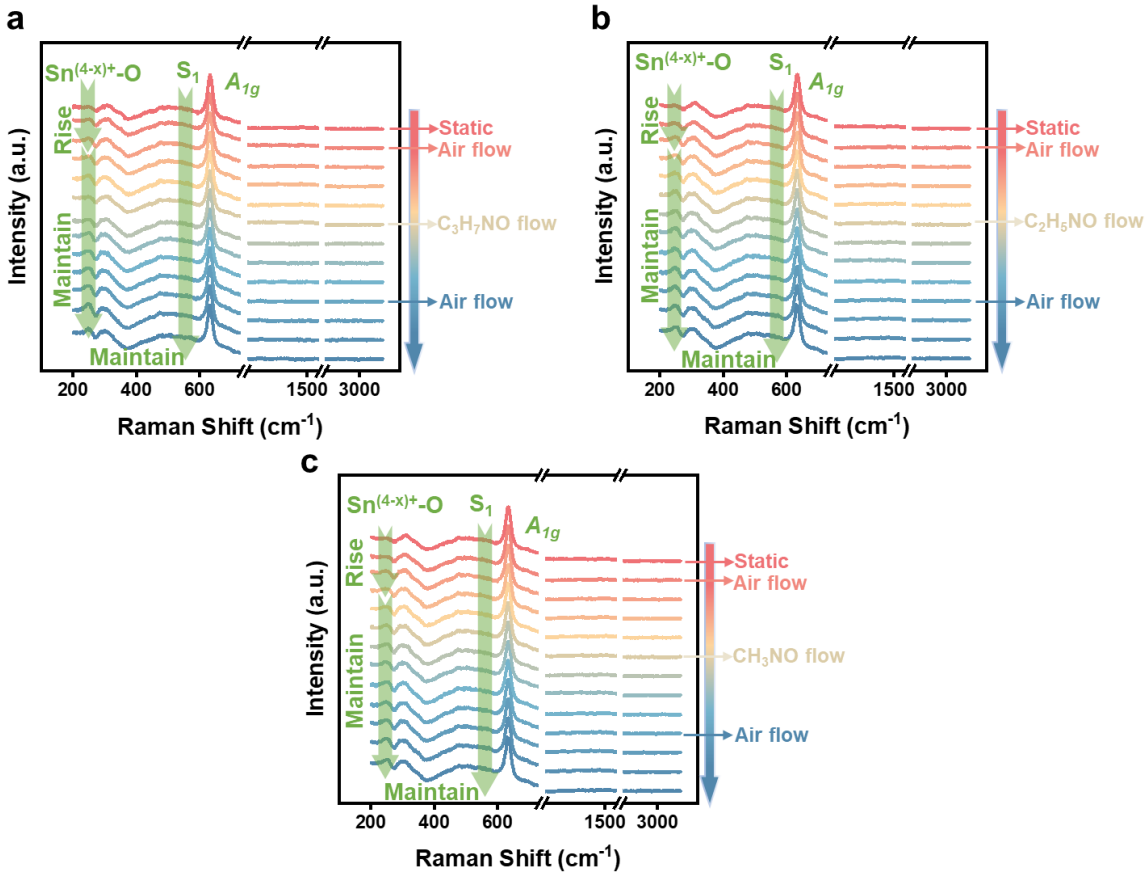

Figure S28. *In situ* Raman spectra of dimethylformamide (a), methylformamide (b) and formamide (c) sensing reactions on SO6.

No Raman features about targeted gases and oxygen species can be observed from these two sensing processes.

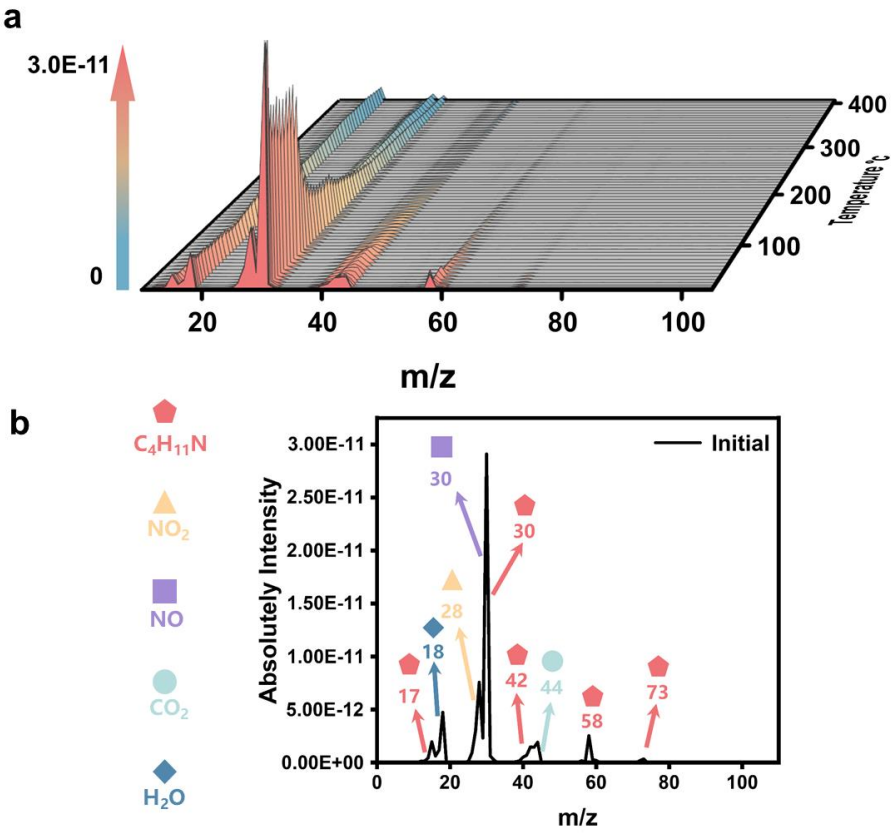

Figure S29. CAD-MS results (a) of diethylamine sensing processes on SO0 during a vacuum condition and the peaks (b) of the m/z attributed to the desorbed gaseous compounds at the initial stage of these processes.

CAD-MS results from the diethylamine-sensing process on SO0 sensor under vacuum conditions reveal peaks of m/z attributed to diethylamine fragments (m/z = 58, 42, 30 and 17) and molecules (m/z = 73) (confirmed by database from National Institute of Standards and Technology , NIST, https://webbook.nist.gov/cgi/cbook.cgi?ID=C109897&Units=SI&Mask=200#Mass-Spec). Meanwhile, mass spectra display information about H_2O, CO_2, NO and NO_2 molecules.

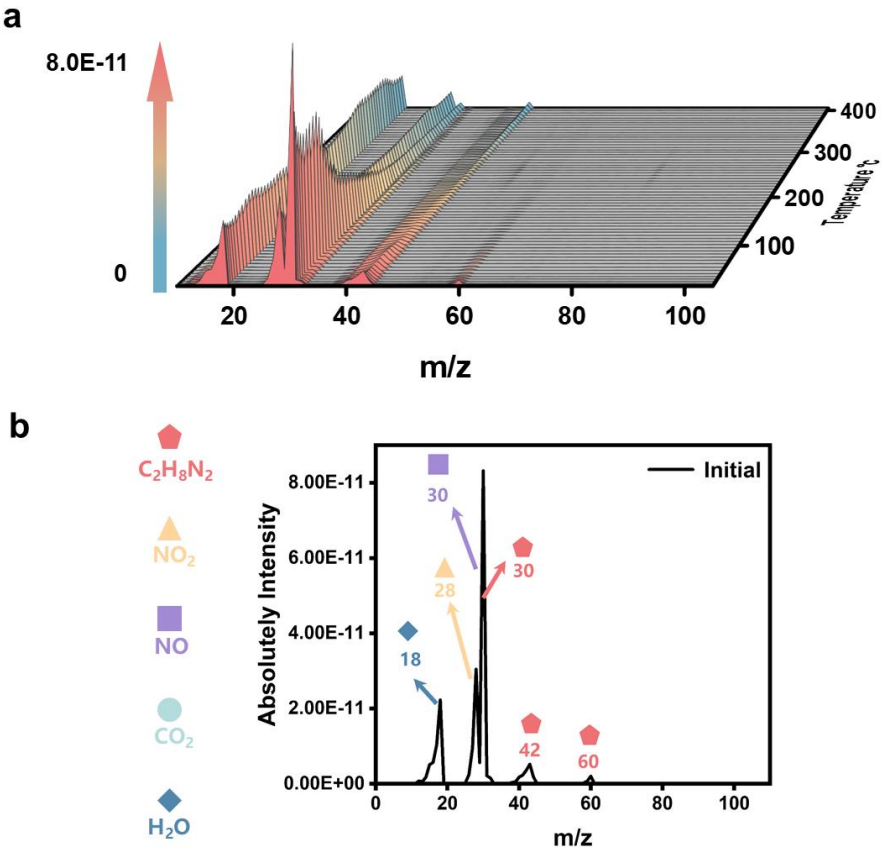

Figure S30. CAD-MS results (a) of ethylenediamine sensing processes on SO0 during a vacuum condition and the peaks (b) of the m/z attributed to the desorbed gaseous compounds at the initial stage of these processes.

CAD-MS results from the ethylenediamine-sensing process on SO0 sensor under vacuum conditions reveal peaks of m/z attributed to ethylenediamine fragments (m/z = 42 and 30) and molecules (m/z = 60) (confirmed by database from National Institute of Standards and Technology , NIST, https://webbook.nist.gov/cgi/cbook.cgi?ID=C107153&Units=SI&Mask=200#Mass-Spec).

Meanwhile, mass spectra display information about H_2O, CO_2, NO and NO_2 molecules.

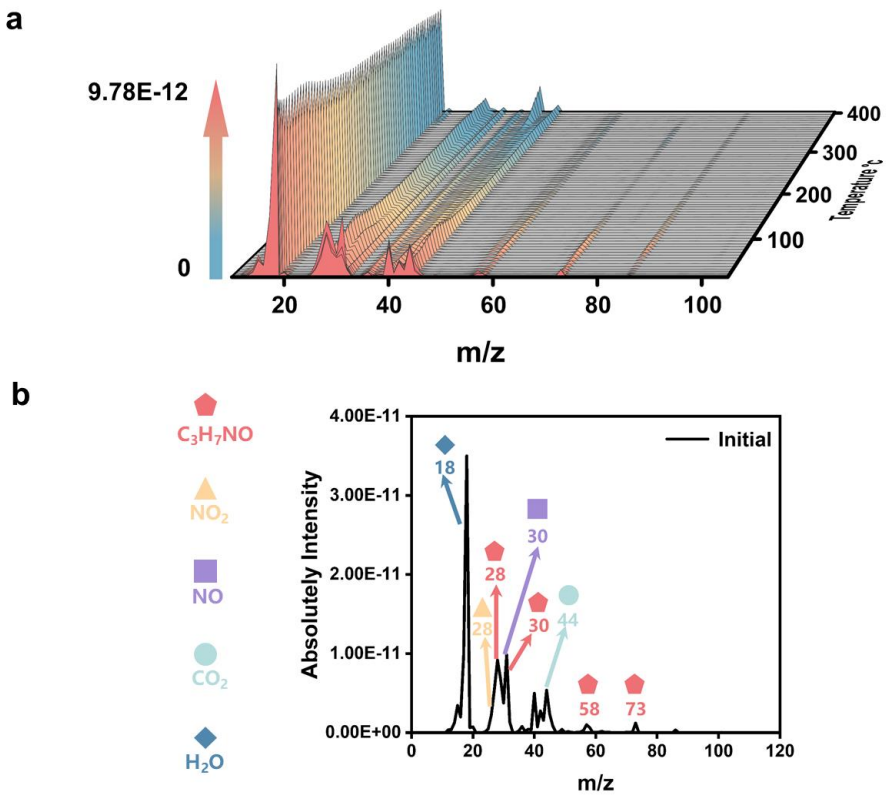

Figure S31. CAD-MS results (a) of dimethylformamide sensing processes on SO0 during a vacuum condition and the peaks (b) of the m/z attributed to the desorbed gaseous compounds at the initial stage of these processes.

CAD-MS results from the dimethylformamide-sensing process on SO0 sensor under vacuum conditions reveal peaks of m/z attributed to dimethylformamide fragments (m/z = 58, 30 and 28) and molecules (m/z = 73) (confirmed by database from National Institute of Standards and Technology, NIST, https://webbook.nist.gov/cgi/cbook.cgi?ID=C68122&Units=SI&Mask=200#Mass-Spec). Meanwhile, mass spectra display information about H_2O, CO_2, NO and NO_2 molecules.

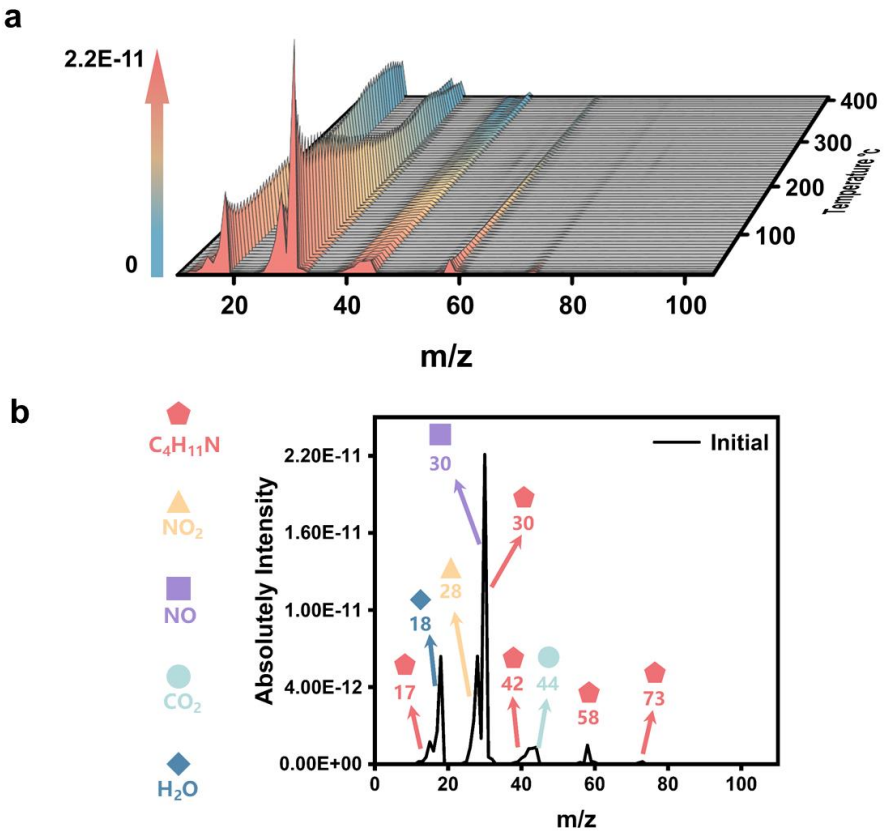

Figure S32. CAD-MS results (a) of diethylamine sensing processes on SO3 during a vacuum condition and the peaks (b) of the m/z attributed to the desorbed gaseous compounds at the initial stage of these processes.

CAD-MS results from the diethylamine-sensing process on SO3 sensor under vacuum conditions reveal peaks of m/z attributed to diethylamine fragments (m/z = 58, 42, 30 and 17) and molecules (m/z = 73) (confirmed by database from National Institute of Standards and Technology , NIST, https://webbook.nist.gov/cgi/cbook.cgi?ID=C109897&Units=SI&Mask=200#Mass-Spec). Meanwhile, mass spectra display information about H_2O, CO_2, NO and NO_2 molecules.

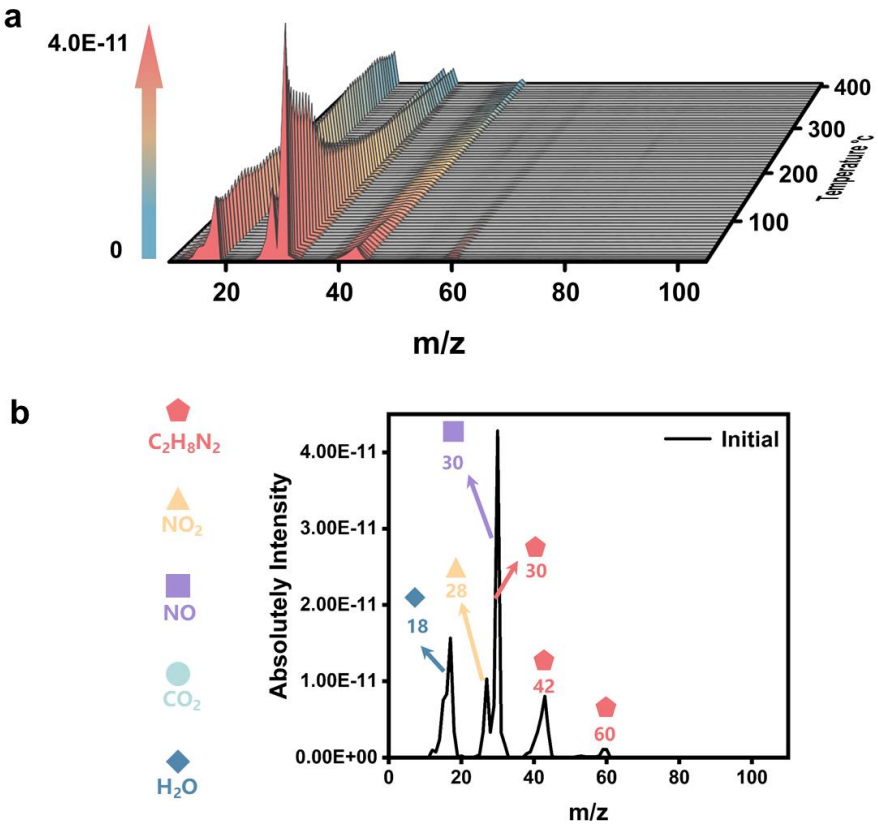

Figure S33. CAD-MS results (a) of ethylenediamine sensing processes on SO3 during a vacuum condition and the peaks (b) of the m/z attributed to the desorbed gaseous compounds at the initial stage of these processes.

CAD-MS results from the ethylenediamine-sensing process on SO3 sensor under vacuum conditions reveal peaks of m/z attributed to ethylenediamine fragments (m/z = 42 and 30) and molecules (m/z = 60) (confirmed by database from National Institute of Standards and Technology, NIST, https://webbook.nist.gov/cgi/cbook.cgi?ID=C107153&Units=SI&Mask=200#Mass-Spec). Meanwhile, mass spectra display information about H_2O, CO_2, NO and NO_2 molecules.

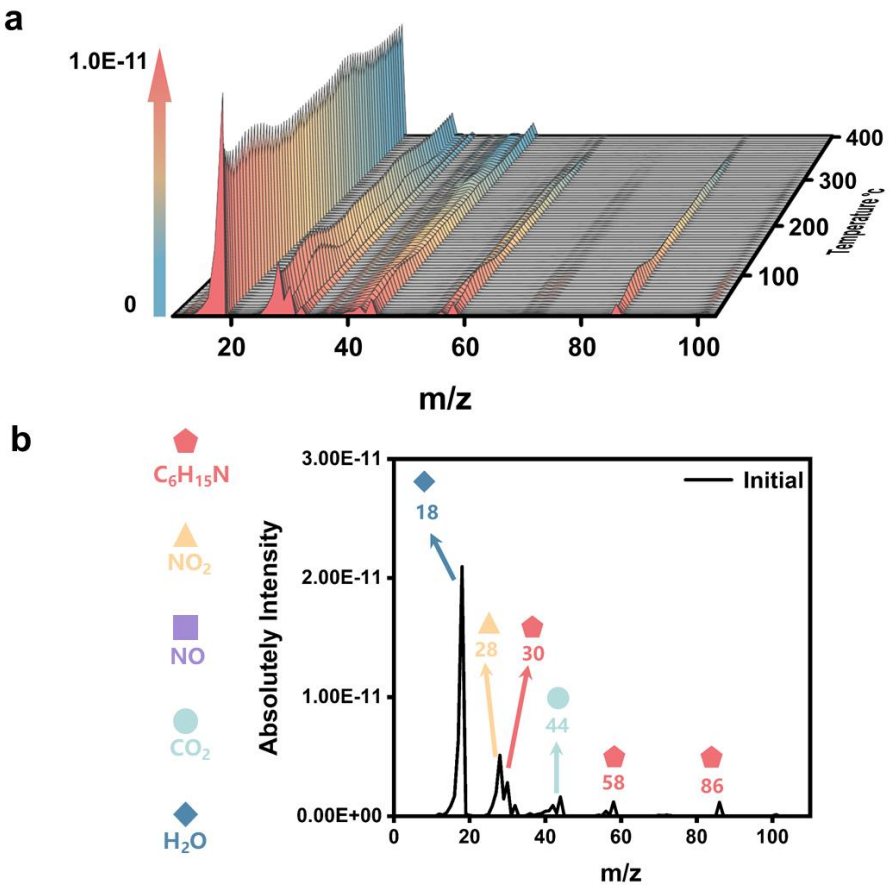

Figure S34. CAD-MS results (a) of triethylamine sensing processes on SO6 during a vacuum condition and the peaks (b) of the m/z attributed to the desorbed gaseous compounds at the initial stage of these processes.

CAD-MS results from the triethylamine-sensing process on SO6 sensor under vacuum conditions reveal peaks of m/z attributed to triethylamine fragments (m/z = 86, 58, 30 and 17) (confirmed by database from National Institute of Standards and Technology, NIST, https://webbook.nist.gov/cgi/cbook.cgi?ID=C121448&Mask=200#Mass-Spec).

Meanwhile, mass spectra display information about H_2O, CO_2 and NO_2 molecules.

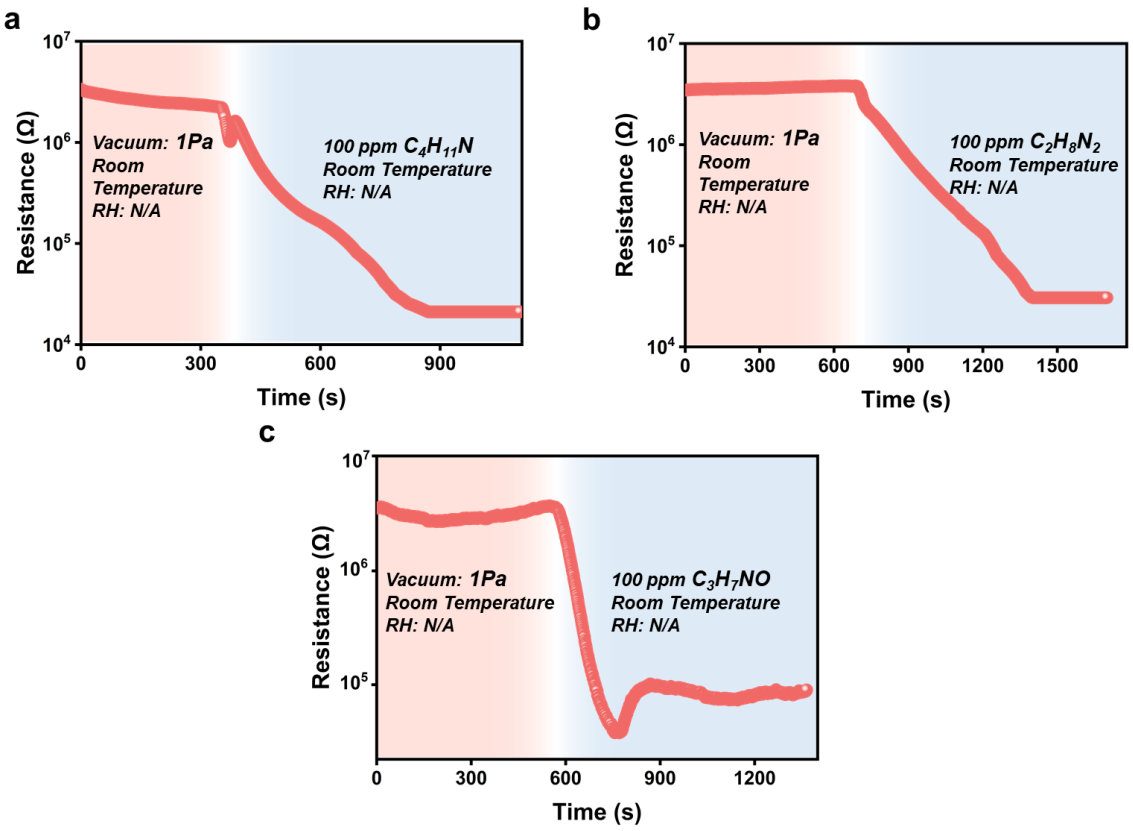

Figure S35. Evolution of SO0 sensor resistance as injection the flow of diethylamine (a), ethanediamine (b) and dimethylformamide (c) gases into vacuum conditions.

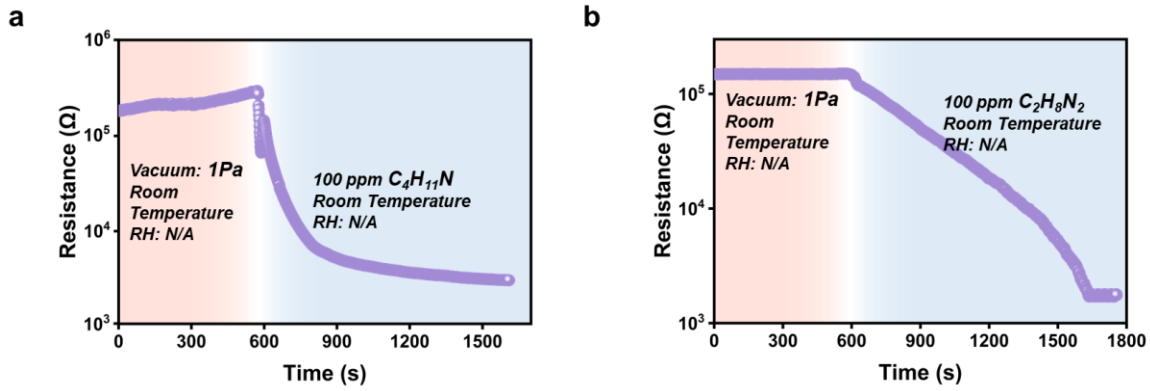

Figure S36. Evolution of SO3 sensor resistance as injection the flow of diethylamine (a) and ethanediamine (b) gases into vacuum conditions.

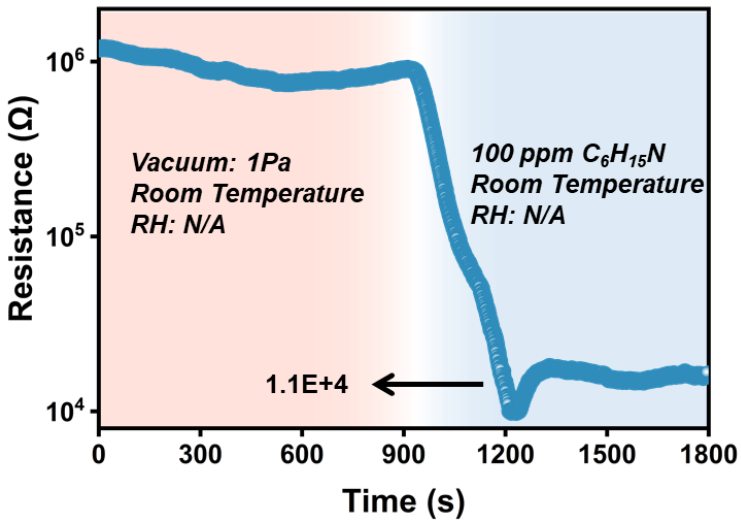

Figure S37. Evolution of SO6 sensor resistance as injection the flow of triethylamine gas into vacuum conditions.

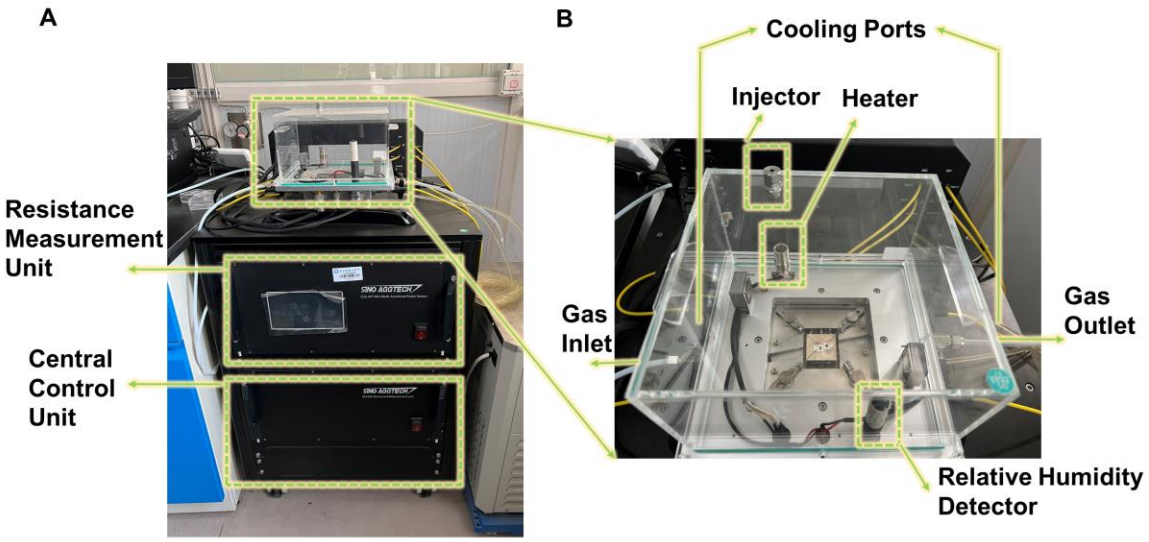

Figure S38. Photo of the device of GS-MT mini-Multi-functional Probe Station (a) and teat chamber (b).

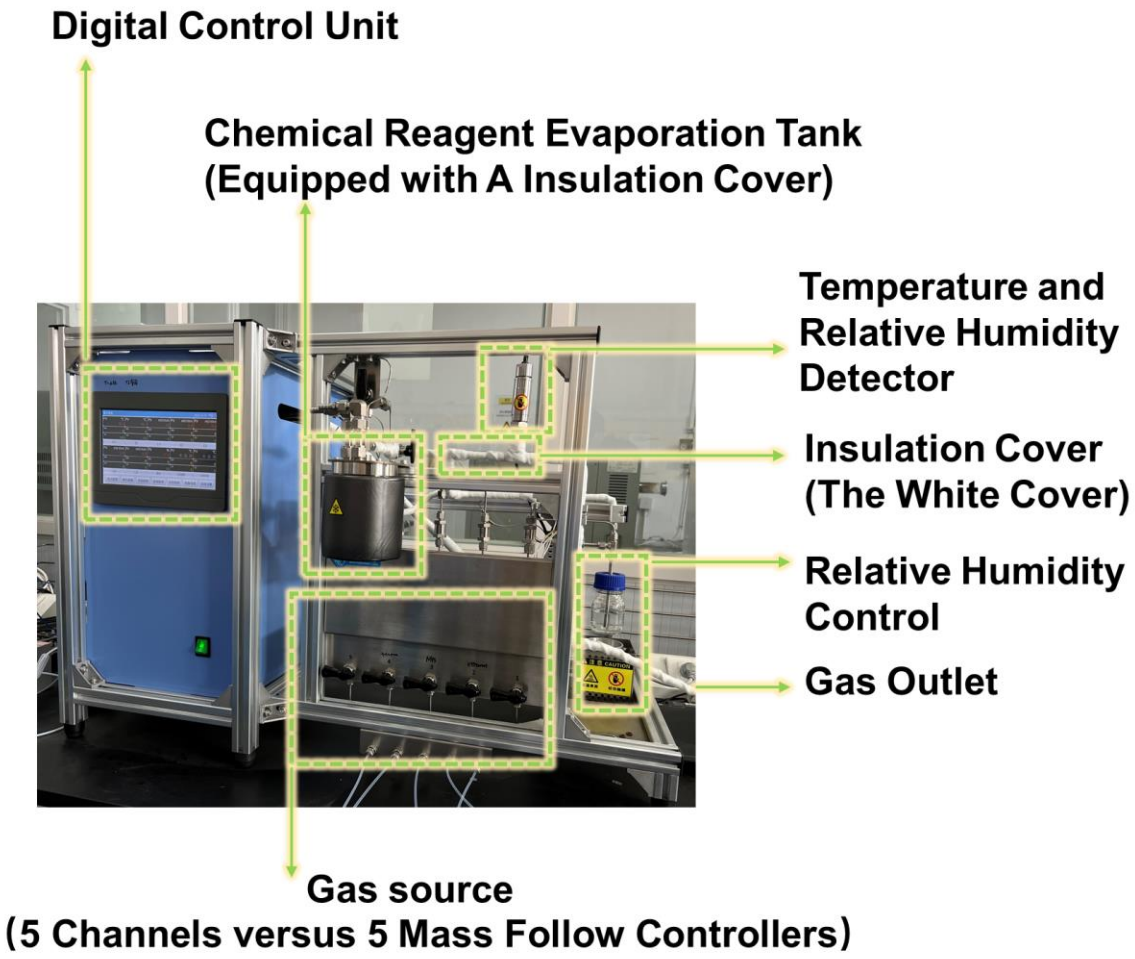

Figure S39. Photo of intelligent gas distribution system.

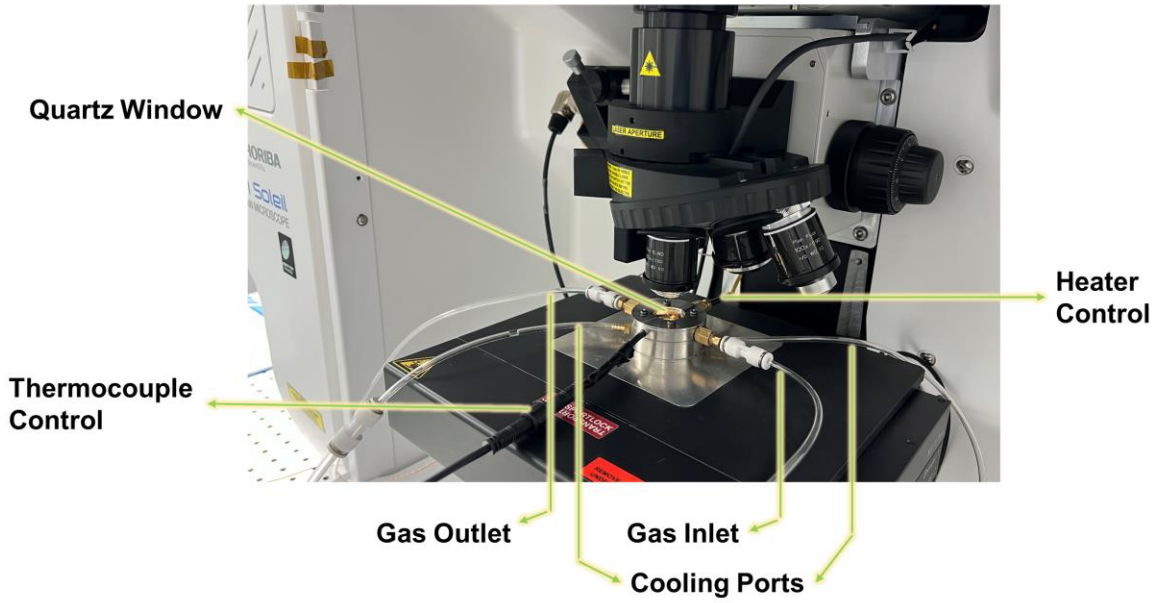

Figure S40. Photo of homemade Raman cell.

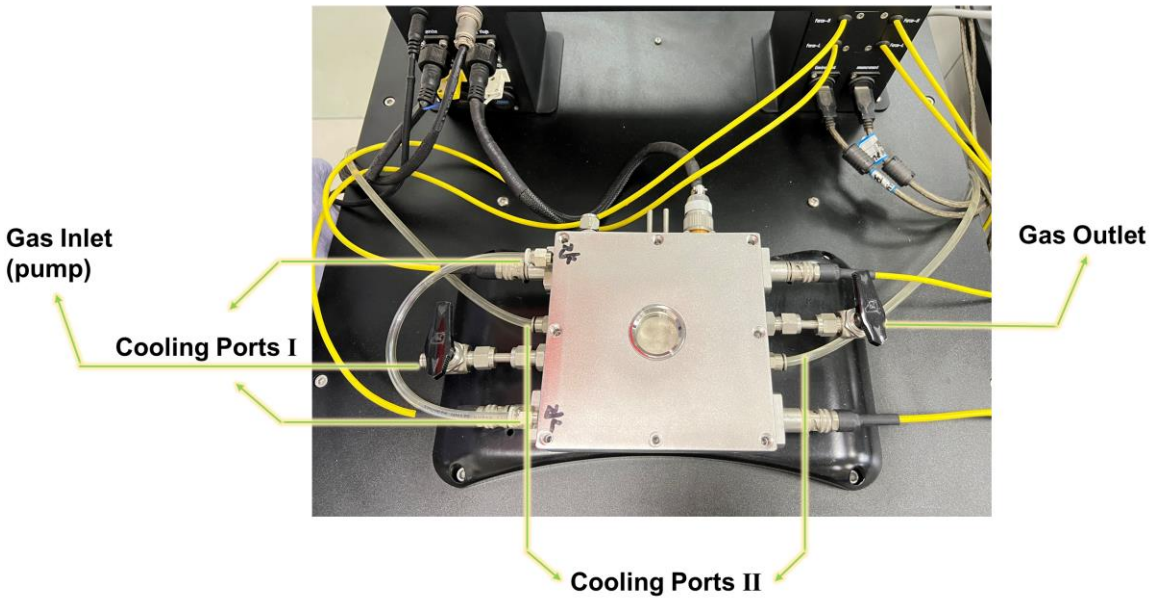

Figure S41. Photo of the customized chamber for electrical resistance measurements under vacuum conditions.

Table S1. Properties of various materials used for triethylamine gas.

Group (reference)	**Material**	**$C_6H_{15}N$ Conc. (ppm)**	**Working Temp. (°C)**	**Gas response (Ra/Rg, Rg/Ra, Ia/Tg)**	**Selectivity (Response ratio)**
Geyu Lu (ACS Sens. 2022, 7, 995−1007)	$NiO/NiFe_2O_4$ fiber-in-tube	50	300	9	1.6
Peng Sun/Geyu Lu (ACS Sens. 2021, 6, 3451−3461)	In_2O_3-NiO composites	100	200	33.9	3.4
Dongjiang Yang/Jun Zhang (ACS Sens. 2017, 2, 897−902)	hollow SnO_2 microfiber	100	50	270	N/A
Jun Zhang (Mater. Horiz., 2020,7, 1519-1527)	Single atom Pt-SnO_2 ultrathin films	10	260	136.2	10.9
Jun Zhang (ACS Appl. Mater. Interfaces 2020, 12, 20704−20713)	porous SnO_2 thin films	10	RT	150.5	79.2
Sandeep Sharma (ACS Sens. 2023, 8, 3146−3157)	$MoSe_2/MoO_3$ Composites	10	20	3	2.78
B. T. Jonker (Nano Lett. 2013, 13, 668−673)	Monolayer MoS_2	100	RT	14.8	1.1
Liuyang Zhang/Jiaguo Yu (Sens. Actuators, B 2021, 331, 129425)	Pt-functionalized ZnO microspheres	100	200	242	60.5

Han Jin/Ling Zang (ACS Sens. 2020, 5, 571−579)	nitrogen-doped carbon shell-coated α-Fe_2O_3 nano-olive	100	260	13.6	4.5
Shantang Liu (Cryst. Growth Des. 2020, 20, 2742−2752)	hierarchical SnO_2 nanostructures	100	70	35.01	11.0
Liping Zhu (Sens. Actuators, B 2022, 368, 132147)	Co_3O_4 films	100	200	230	2.3
Peng Song (Sens. Actuators, B 2023, 379, 133239)	ZnO/MoO_3 heterostructures	50	180	280	62.2
Guodong Wang (Sens. Actuators, B 2021, 343, 130126)	PdO-ZnO-In_2O_3 nanofibers	50	250	386	51.5
Sukhwinder Singh/Hyoun Woo Kim (ACS Sens. 2020, 5, 571−579)	Multiwalled Carbon Nanotubes	10	RT	10	2.5
Shun Mao (ACS Sens. 2022, 7, 1874−1882)	Pt-Functionalized $Ti_3C_2T_x$	10	RT	6	3
Lihua Huo (Sens. Actuators, B 2015, 208, 406-414)	α-MoO_3	100	250	416	2.2
Zhi Yang (Sens. Actuators, B 2020, 306, 127536)	hierarchical WO_3	10	205	11.6	5
This Work	**SnO_2 with OV_{Bri}**	**100**	**RT**	**19938.92**	**20000 to interfering gases;**

					123.1 to amine gases

Table S2. Properties of various materials used for diethylamine gas.

Group (reference)	**Material**	**$C_4H_{11}N$ Conc. (ppm)**	**Working Temp. (°C)**	**Gas response (Ra/Rg, Rg/Ra, Ia/Tg)**	**Selectivity (Response ratio)**
Qiuhong Li (RSC Adv.,2016,6,6511)	V_2O_5-decorated a-Fe_2O_3 composite nanorods	100	350	8.9	7.4
Guobao Xu /Wei Chen (Anal. Chem. 2022, 94, 15359−15366)	Pd Doping in Ni-P_2O_5/MoO_3 Hollow Polyhedral Heterostructures	10	175	42.5	8.5 to interfering gases; 3.4 to amine gases
Guobao Xu /Wei Chen (Anal. Chem. 2023, 95, 17568−17576)	1D CuO Nano-Ellipsoids	15	RT	23	39.16 to interfering gases; 2.79 to amine gases
Guobao Xu /Wei Chen (Anal. Chem. 2023, 95, 1747−1754)	$Ni_{0.4}Fe_{2.6}O_4$ Nanorice	5	175	23	N/A
This Work	**SnO_2 with OV_{Bri}**	**100**	**RT**	**123.41**	**123 to interfering gases; 1.3 to amine gases**

Table S3. Properties of various materials used for ethanediamine gas.

Group (reference)	**Material**	**$C_2H_8N_2$ Conc. (ppm)**	**Working Temp. (°C)**	**Gas response (Ra/Rg, Rg/Ra, Ia/Tg)**	**Selectivity (Response ratio)**
Abliz Yimit (Sensors, 2017, 17, 2717)	Tetrakis (4-Nitrophenyl) Porphyrin	100	RT	975	1.57 to interfering gases; 7.06 to amine gases
This Work	**SnO_2 with OV_{Bri} strcture**	**100**	**RT**	**161.91**	**161 to interfering gases; 1.3 to amine gases**

SI References

(1) Kılıç, Ç.; Zunger, A. Origins of Coexistence of Conductivity and Transparency in SnO_2. *Phys. Rev. Lett.* **2002,** *88*, 095501.

(2) Xu, K.; Tian, S.; Zhu, J.; Yang, Y.; Shi, J.; Yu, T.; Yuan, C. High Selectivity of Sulfur-Doped Sno2 in No2 Detection at Lower Operating Temperatures. *Nanoscale* **2018,** *10*, 20761-20771.

(3) Chang, H.-C.; Jiang, J.-C.; Tsai, W.-C.; Chen, G.-C.; Chang, C.-Y.; Lin, S. H. The Effect of Pressure on Charge-Enhanced C–H···O Interactions in Aqueous Triethylamine Hydrochloride Probed by High Pressure Raman Spectroscopy. *Chem. Phys. Lett.* **2006,** *432*, 100-105.

(4) Gamer, G.; Wolff, H. Raman and Infrared Spectra of Gaseous Secondary Aliphatic Amines [$(CH_{32}NH$, $(CH_3)_2ND$, $(C_2H_5)_2NH$ and $C_2H_5NHCH_3$]. *Spectrochim. Acta, Part A* **1973,** *29*, 129-137.

(5) Cáceres, M.; Lobato, A.; Mendoza, N. J.; Bonales, L. J.; Baonza, V. G. Local, Solvation Pressures and Conformational Changes in Ethylenediamine Aqueous Solutions Probed Using Raman Spectroscopy. *Phys. Chem. Chem. Phys.* **2016,** *18*, 26192-26198.

(6) Xuan, X.; Zhang, H.; Wang, J.; Wang, H. Raman Spectroscopic and DFT Studies on Solutions of $NaBF_4$ in N,N-Dimethylformamide. *J. Raman Spectrosc.* **2003,** *34*, 465-470.